Manuscript
Click here to view linked References
https://doi.org/10.1016/j.combustflame.2018.08.002
This is the Pre-Published Version.

Mass Interminglement and Hypergolic Ignition of TMEDA and WFNA Droplets by Off-center Collision

Dawei Zhang[1,#], Chengming He[1,#], Peng Zhang[1*], Chenglong Tang[2]

1. Department of Mechanical Engineering
The Hong Kong Polytechnic University, Kowloon, Hong Kong

2. State Key Laboratory of Multiphase Flow in Power Engineering
Xi'an Jiaotong University, Xi'an, 710049, China

* Corresponding author
E-mail address: pengzhang.zhang@polyu.edu.hk (P. Zhang)
# The authors equally contributed to the work.

© 2018. This manuscript version is made available under the CC-BY-NC-ND 4.0 license https://creativecommons.org/licenses/by-nc-nd/4.0/

Abstract

Binary collision between a smaller N, N, N', N'- tetramethylethylenediamine (TMEDA) droplet and a larger white fuming nitric acid (WFNA) droplet was investigated experimentally and computationally for understanding the influence of off-center collision on the hypergolic ignitability of the system, which is controlled by the mass interminglement and mixing subsequent to the droplet coalescence. The ignition delay time was experimentally found to non-monotonically vary with the impact parameter, which measures the degree of off-center collisions. This phenomenon was hypothetically attributed to the non-monotonicity of mass interminglement of colliding droplets with increasing the impact parameter—the increased droplet stretching by slightly off-center collision promotes mass interminglement, but the stretching separation by significantly off-center collision reduces mass interminglement. This hypothesis was computationally verified by a validated volume-of-fluid (VOF) simulation of a simplified problem, in which the transport phenomena and chemical reactions are neglected and the controlling physics of droplet mass interminglement is emphasized. Furthermore, a parametric study for wide ranges of controlling non-dimensional parameters, such as the collision Weber number of 20-140 and the droplet size ratio of 1.3-2.0, further confirms that the non-monotonicity of ignition delay time with the impact parameter is a general characteristic of the present hypergolic system.

Keywords: Hypergolic ignition; TMEDA; WFNA; Droplet collision; Impact parameter; Volume-of-Fluid

Nomenclature

Physical quantities

D	droplet diameter
t	physical time
t_{ine}	characteristic collision time, $t_{\mathrm{ine}} = D_L/U$
t_{osc}	characteristic oscillation time of the larger droplet, $t_{\mathrm{osc}} = \sqrt{\rho_L D_L^3/\sigma_L}$
U	experimental relative velocity between the two colliding droplets in the x-direction
α	mass diffusivity
μ	dynamic viscosity
ρ	density
σ	surface tension coefficient
χ	projection of the distance between two droplet mass centers along the direction of U

Numerical parameters

C	time-dependent dye function concentration ϕ in the merged droplet, $C = \frac{\lvert\phi-0.5\rvert}{0.5} C_0$
C_0	dye function concentration ϕ in the initially unmixed droplets, $C_0 = \begin{cases} 0, & \phi = 0 \\ 1, & \phi > 0 \end{cases}$
C_∞	dye function concentration ϕ in the fully mixed droplets, $C_\infty = 1/(1+\Delta^3)$
f	Volume-of-fluid (VOF) function
H	Heaviside function
R	local mesh refinement level
V	total volume of fluid droplets
ϕ	mass dye function with $\phi = 1$ in the smaller droplet otherwise $\phi = 0$

Experimental parameters

B	impact parameter, $B = 2\chi/(D_S + D_L)$
G	threshold value of the grayscale levels
N	pixel number of the entire image
N_d	total pixel number of the grayscale levels below G_{low}
N_b	total pixel number of the grayscale levels above G_{high}
r	ratio of the pixel number (N_b or N_d) to the total pixel number (N)

Non-dimensional and normalized variables

M	mixing index, $M = 1 - \frac{\int_V \lvert C-C_\infty\rvert H(f-1)\mathrm{d}V}{\int_V \lvert C_0-C_\infty\rvert H(f-1)\mathrm{d}V}$

Oh Ohnesorge number, $Oh = \mu_L/\sqrt{\rho_L \sigma_L D_L}$

Pe Peclet number, $Pe = UD_L/\alpha$

$\tilde{Q}$ dimensionless fluid-dynamical quantities of interest

T non-dimensional time, $T = t/t_{\mathrm{osc}}$

We Weber number, $We = \rho_L D_L U^2/\sigma_L$

Δ size ratio of the larger droplet to the smaller droplet, $\Delta = D_L/\, D_S$

Subscripts

b species have the grayscale levels above G_{high} with $r_b = N_b(t|G > G_{high})/N$

d species have the grayscale levels below G_{low} with $r_d = N_d(t|G < G_{low})/N$

g fluid properties of the surrounding gas (air) environment

high higher threshold value of the grayscale levels, $G_{\mathrm{high}} = 250$

L fluid properties of the larger (WFNA) droplet

low lower threshold value of the grayscale levels, $G_{\mathrm{low}} = 5$

S fluid properties of the smaller (TMEDA) droplet

1. Introduction

1.1. Hypergolic Ignition by Head-on Collision of TMEDA and WFNA Droplets

Spontaneous ignition of hypergolic liquid propellants occurs upon their contact without an external source of energy [1-4]. Hypergolic propellants and ignition have received lasting attentions in the past decades for their applications in rocket propulsion, particularly when multiple engine restarts are required [3]. Unlike the auto-ignition of a homogeneous gaseous mixture of non-hypergolic reactants, hypergolic ignition is intrinsically heterogeneous as it involves mixing and reaction of initially separated propellants in both liquid phase and gas phase [5-9].

Existing experimental methods for studying hypergolic ignition differ in the mode and extent of liquid-phase mixing [1, 2]. Specifically, the piston-driven apparatus for rapid mixing of liquid reactants is designed to minimize the mixing effect in liquid phase [10-13]. Designed for variable testing conditions, the impinging jet apparatus [7, 14-16] often employs partially mixing reactants. In recent years, the drop test [8, 17] has been widely used as a fast tool to prescreen potential hypergolic propellants. In a typical drop test, a free or suspended propellant drop is made to impact the liquid pool of another propellant [18, 19], which is either confined in a container or placed on a solid surface. Although these test systems help researchers obtain a lot of valuable understanding on hypergolic ignition [7, 8, 17, 19], they have a common deficiency — it is generally difficult to quantify the system-dependent liquid-phase mixing owing to the unavoidable "wall effect" by the jet nozzle or the container or the surface.

Motivated by studying the hypergolic ignition initialized by the collision of freely moving propellant droplets and hence free from "wall effect", the authors recently established and conducted the experiment of binary droplet collision of N,N,N',N' – tetramethylethylenediamine (referred to as TMEDA hereinafter) and white fuming nitric acid

(referred to as WFNA hereinafter) in atmospheric environment [20]. This preliminary experimental study was focused on verifying the applicability and reliability of the established experimental apparatus for studying hypergolic ignition triggered by binary droplet collision and on the special (also nontrivial) situation of head-on collision. The significance of the experiment can be appreciated by recognizing that binary droplet collision could be a frequent event in the combustion chamber of rocket engines, where liquid propellants are injected into and quickly atomized into droplets. Furthermore, the recent interests in gelled hypergolic propellants (GHP) further stress the need for such an experiment because the substantially reduced volatility by gelling suppresses the droplet vaporization and therefore the ignition of GHPs heavily relies on the liquid-phase mixing [21, 22]. It is known that the rapid mixing of reactants promotes the reaction rate of a non-premixed system. It is also true for the present system consisting of hypergolic fuel and oxidizer, where the enhancement of liquid-phase mass interminglement between droplets reduces the ignition delay time. The previous studies [1, 7] have observed that the ignition delay time is closely related to the initial contact and subsequent mixing between hypergolic fuel and oxidizer droplets.

In order to focus on understanding the influence of droplet mixing on the hypergolic ignition and to avoid dealing with many factors at a time, the authors deliberately limited the scope of their previous experimental study [20] to the head-on collision at variable collision Weber number ($We = 20 - 220$) and droplet size ratio ($\Delta = 1.2 - 2.9$), but at a fixed Ohnesorge number ($Oh = 2.5 \times 10^{-3}$) by fixing the size of the WFNA droplet. The TMEDA/WFNA hypergolic system was chosen for the study because it has been recently proposed as a promising substitute for the highly toxic hydrazine propellants. The experimental method can be applied to study other hypergolic systems. The most notable experimental discovery in the study is the non-monotonic variation of hypergolic ignition

delay time with increasing We. The underlying physics is the non-monotonic emergence of a "jet-like" internal mixing within the coalesced droplet with increasing We, a fluid dynamical phenomenon that was recently identified by Tang *et al.* [23] in unequal-size droplet collision. The "jet-like" internal mixing facilitates the exothermic liquid-phase reaction, TMEDA + $2HNO_3 \rightarrow$ TMEDADN, whose heat release is crucial to the subsequent droplet heating and vaporization, the decomposition of the propellants, and eventually the gas-phase ignition [7, 8]. Another notable experimental discovery is that Δ significantly affects the hypergolic ignition mainly by changing the available mass of the propellants participating the chemical reaction, while it also affects the droplet mass interminglement and therefore liquid-phase mixing.

1.2. Off-center Collision and Mixing of Binary Droplets

In spite of the above findings about the hypergolic ignition by the head-on collision of TMEDA and WFNA droplets, it should be recognized that head-on collision is a rare event in reality and that off-center collisions are significantly more frequent. Figure. 1 illustrates the off-center collision of two droplets of diameters D_S and D_L (the subscript "*S*" denotes the smaller droplet and "*L*" the larger one). The impact parameter, $B = 2\chi/(D_S + D_L)$, measures the deviation of droplet trajectory from the head-on situation and is defined as the ratio of the projection of the separation distance of two droplet centers in the direction of their relative velocity, χ, to the sum of the two droplet radii, $(D_S + D_L)/2$. Head-on collision occurs at $B = 0$, grazing collision at $B = 1$, and off-center collision at $0 < B < 1$. The relative importance of droplet inertia to its surface tension is characterized by the collision Weber number, $We = \rho_L D_L U^2/\sigma_L$, and the effects of the size disparity by the size ratio, $\Delta = D_L/D_S$.

Most previous droplet collision experiments were focused on identifying various collision outcomes and quantifying the effects of various controlling parameters, summarized by Orme [24] and Brenn [25]. Although the identified collision outcomes, such as bouncing,

coalescence, separation and splashing, depend on not only We, B and Δ but also the ambient pressure and other liquid properties [26, 27], it can be generally concluded that bouncing occurs at relatively small $We \sim O(1)$, splashing occurs at sufficiently large $We \sim O(10^2)$, and coalescence and separation occur at intermediate $We \sim O(10)$.

Figure 1 shows the droplet collision nomogram in the $We - B$ parameter space. The outcomes of droplet collision at fixed We and Δ but different Bs are schematized in Cases (i), (ii) and (iii). For head-on collision depicted by Case (i), the two colliding droplets exhibit axisymmetric impaction and oscillation, and result in permanent coalescence. With increasing B to affect the off-center collision depicted by Case (ii), the coalesced droplets exhibit increasingly asymmetric impaction and stretching. At sufficiently large B depicted by Case (iii), the intensely stretched droplet is eventually separated into two major droplets with a certain number of tiny satellite droplets.

The mixing of two colliding droplets is an important aspect of binary droplet collision and has recently gained increasing interests for its practical relevance in microfluidics and GHP systems. In consideration of that the head-on collision of identical droplets produces minimal mixing owing to its intrinsic "symmetry" in geometry and physical properties, researchers have employed "symmetry breaking" to enhance mixing by introducing size disparity [23, 28-30], non-Newtonian effect [31-34], and Marangoni effect [35, 36] to droplet collision. Off-center collision, which breaks the geometric symmetry of head-on collision, has however not been sufficiently studied for its influence on droplet mixing, probably because the characterization and quantification of its intrinsically three-dimensional nature is challenging for both experiment and simulation.

In the early experimental study of Ashgriz and Poo [28], the inter-droplet mass exchange was observed after the stretching separation. Inamuro *et al.* [37] used the lattice

Boltzmann method (LBM) to simulate the equal-size droplet collision at $We = 80$ and various Bs. By tracing massless colored particles originally embedded in the two droplets, they defined a mixing rate as the percentage of the number of particles of a color in the total number of particles in a droplet. The mixing rate was found to non-monotonically vary with B, and the maximum mixing rate is about 30% at about $B = 0.2$. In another LBM study of Sakakibara and Inamuro [38] on the collision of unequal-size droplets, they observed mixing enhancement by increasing We at $\Delta = 2$ and $B = 0$, but did not report any results on the mixing rate for off-center collision.

Sun et al. [39] numerically studied the off-center collision of two identical droplets by using the moving particle semi-implicit method. Although their results show significant discrepancies compared with the previous experiments on collision outcomes, the non-monotonic variation of the mixing rate with B was observed at $We = 1.5$. A similar result was also obtained in the Volume-of-Fluid (VOF) simulation of Chen *et al.* [40] on the energy and mass transfer between two equal-size droplets with We being up to 70. Particularly, they found that the maximum mass transfer rate appears at about $B = 0.3{\sim}0.4$, being consistent with Inamuro *et al.*'s results.

1.3. Motivations and Scopes of the Present Study

The previous results on the non-monotonic droplet mixing rate with varying B inspired the authors to conduct the present experimental and numerical study on the off-center collision of TMEDA and WFNA droplets of unequal sizes. There are a few remarks about the motivations and scopes of the present study.

First, the non-monotonic variation of the droplet mixing rate with B implies that there might exist a corresponding non-monotonicity of hypergolic ignition delay. The present study aims to not only contribute a worthy, significant enrichment to the previous experimental

observations limited to head-on collisions, but also embrace complex, interesting fluid physics that demands additional computational investigations.

Second, to avoid the unnecessary complexity of phenomenological description and to facilitate the comparison with head-on collision, the present experimental study was first focused on the representative situation at fixed $We = 60.9$ and $\Delta = 1.6$ but at various B, and then extended to other We and Δ. The Ohnesorge number, which measures the relative importance of droplet viscous force compared with droplet inertia and surface tension, was still fixed at $Oh = 2.5 \times 10^{-3}$ in the present study by fixing the size of the WFNA droplet. The influence of Ohnesorge number, or more generally, the droplet size effects, merit future studies but will not considered in the present one.

Third, to help understand the present experimental observations, we conducted the VOF simulation of the off-center collision of non-reacting droplets, with emphasis on investigating the influence of B on droplet mixing. Similar simulations have been reported in literature for either equal-size droplets or head-on collisions, but not for the off-center collision of unequal-size droplets. It should be noted that we had no an ambition to simulate the extremely complex and tangled physicochemical processes of hypergolic ignition of TMEDA and WFNA droplets, including the fluid-dynamical processes of droplet collision and mixing, the transport processes of mass diffusion and droplet heating, the phase change process of droplet vaporization, and the chemical processes in liquid and gas phases. Based on the results from the previous study [20], the hypergolic ignition delay concerned in the present problem dominantly depends on the early stage of droplet interaction characterized by the fluid-dynamical processes of droplet collision and mixing. Consequently, the present VOF simulation, which has been sufficiently validated against available experiments in literature, is able to provide useful information about the early stage of droplet interaction, when the physical transport, phase change and chemical reactions have not fully emerged yet.

Based on the above considerations, we present the present study as follows. The experimental apparatus and methodology are described in Section 2, followed by the expatiated VOF method and experimental validation, in Section 3. Internal mass interminglement and hypergolic ignition of TMEDA and WFNA droplets under slightly off-center conditions are presented and analyzed, by the use of the VOF simulation of a simplified problem, in Section 4. As increasing the impact parameter to effect droplet stretching separation, the moderately off-center and nearly grazing collisions are presented and analyzed, in Section 5 and Section 6, respectively. The correlation between the quantitative mixing index and the ignition delay time is presented, in Section 7, followed by the discussion about the parametric study of We and Δ, in Section 8.

2. Experimental Specifications

The schematic of the experimental apparatus used in the present study, as shown in Fig. 2, has been expatiated in the authors' previous paper [20] and therefore will not be repeated here. To briefly describe the apparatus, droplets are generated by two independently controlled droplet generators, and each of which is mounted on a XYZ microscope stage with a precision of 2 μm. Each droplet generator is connected to a liquid tank, from which the pressurized nitrogen gas drives the liquid to the generator. For generating WFNA droplets with strong corrosiveness, an in-house needle-shape nozzle was made of the anti-corrosion material of Teflon (Polytetrafluoroethylene). Just as the WFNA droplet size was fixed at 1.45 mm for fixing the Ohnesorge number [20], so the same size was used in the present study.

It is noted that the Weber numbers in the previous hypergolic ignition experiments are of $O(1) - O(10^2)$ for drop tests [17, 19], and of $O(10^3)$ for jet impinging tests [15, 41]. The droplets used in prevailing droplet collision experiments [8, 17, 19, 20] (including the present

study) are within the range of $O(0.1) - O(1)\ mm$, which are larger than the droplets in real engines. However, according to the similarity law of fluid dynamics, the non-dimensional parameters, such as the Weber number, the size ratio, and the impact parameter, but not the dimensional droplet sizes, control the phenomena concerned in the present study. Adopting relatively large droplets in the experiment is justifiable as long as the sphericity of the droplets is ensured and the non-dimensional parameters are under control. The Weber number range considered in the present study is in the range of 20-140. The experiments at higher Weber numbers will be considered in our future studies.

The electromagnetic micro-valve made by Fritz Gyger AG was employed to generate TMEDA droplets whose sizes vary from 0.2mm to 1.5 mm. Temporally and spatially stable collisions between the TMEDA and WFNA droplets were realized by precisely adjusting the tunable droplet generation time and the position of XYZ stage.

High speed camera Phantom V711 was utilized to record shadowgraph images of the collision and ignition processes with a fixed sampling rate of 5000fps and a fixed shutter time of 5 μs. With the enlarging optical lenses, each shadowgraph image records a spatial region of 4cm×3cm, in which there are 1024×800 pixels and each pixel is resolved by 40 μm ×40 μm. A MATLAB program was developed to analyze the images to determine the diameters, the impact velocities, and the impact parameter of the droplets, as shown in Fig. 3. The measurement error for droplet diameters is one pixel and less than 7%. The impact parameter can be determined with a relative error of less than 7%. The uncertainty of measured droplet velocity, which is determined by averaging the displacement of the droplet center during five successive images (i.e. 1.0ms), is about 3%-8%.

A grayscale analysis of the shadowgraph images was proposed in the authors' previous study [20] to precisely determine the ignition delay time with an uncertainty of less than 0.2 ms. The analysis is based on that there are distinctly different grayscale levels (0-256)

in the shadowgraph images, that the darkest areas are occupied by droplets and their vapors have levels lower than 5, and that the brightest areas occupied by luminous ignition kernels and flames have levels higher than 250. The reliability and accuracy of the grayscale analysis has been verified by the measurements of visible lights and infrared radiation [20].

3. Numerical Methods and Experimental Validations

3.1 Problem Definition and Simplification

As discussed in Section 1.3, the present VOF simulation aims to characterize the droplet mixing in the early stage of collision between TMEDA and WFNA droplets. The physical properties of the liquid propellants are given in Table 1 in comparison with those of water. Several assumptions and simplifications were made in the simulation and are expatiated as follows.

Table 1. Physical properties of various liquids

Liquids	Surface tension, σ (10^{-2} N·m^{-1})	Viscosity, μ (10^{-3} N·s·m^{-2})	Density, ρ (10^{3} kg·m^{-3})
TMEDA	2.65	0.90	0.78
WFNA	5.86	0.89	1.50
Water	7.29	1.00	1.00

First, the liquid-phase and gas-phase reactions, the droplet heating, and the droplet vaporization are negligible in the early stage. This is because the early stage lasts for about a few milliseconds and is significantly shorter than the hypergolic ignition delay time, which is typical of some tens of milliseconds [10-13]. As a result, the present simulation problem can be first simplified as the off-center collision of two unlike droplets, where the flows in both liquid- and gas-phases are incompressible, non-reactive, and isothermal. The flow incompressibility for liquid-phase droplets is self-evident. The gas-phase flow due to vaporization (Stefan's flow), the heat and mass transport, and the flame propagation are

sufficiently slow so that the compressibility effect is negligible. Dimension analysis indicates that a physical quantity of interest, denoted by $\tilde{Q}$, depends on nine non-dimensional parameters as

$$\tilde{Q} = f\left(We, B, \Delta, Oh, \frac{\rho_S}{\rho_L}, \frac{\mu_S}{\mu_L}, \frac{\sigma_S}{\sigma_L}, \frac{\rho_g}{\rho_L}, \frac{\mu_g}{\mu_L}\right) \quad (1)$$

Second, the effects of the density difference and the viscosity difference between the droplets can be neglected. Because the Peclet number, $Pe = UD_L/\alpha$, is as large as $O(10^6)$ in the present problem, the droplet mixing in the early stage is dominated by collision-induced flow convection in lieu of the liquid-phase mass diffusion. It is also noted that TMEDA and WFNA has very similar viscosity so that $\mu_S/\mu_L \approx 1$.

Third, the droplet mixing induced by the surface tension variation, also known as the Marangoni effect, can be neglected. This is because the capillary pressure driven by the surface tension difference, $|\sigma_S - \sigma_L|/D_L$, is substantially smaller than the droplet dynamic pressure, $\rho_L U^2$. The ratio of these two pressures yields

$$\frac{|\sigma_S - \sigma_L|/D_L}{\rho_L U^2} \sim \frac{|\sigma_S/\sigma_L - 1|}{We} \sim O(10^{-2}) \quad (2)$$

Finally, $\rho_g/\rho_L \sim O(10^{-3})$, $\mu_g/\mu_L \sim O(10^{-2})$, and $Oh = 2.5 \times 10^{-3}$ are fixed in the present problem because we considered the collisions between TMEDA droplets of varying diameters with WFNA droplets of a fixed diameter of 1.45mm in atmospheric air. Previous studies [23, 30, 33, 34] have proved that the small gas-liquid density and viscosity ratios have negligible influence on the droplet internal flow.

With the above simplifications and assumptions, the present simulation problem is further simplified as the off-center collision of two droplets of the same liquid, leading to only three controlling non-dimensional parameters, namely, We, Δ and B. The simulation results are the same for any fluids as long as their physicochemical properties satisfy the

above approximations and they have the same set of the non-dimensional parameters. As will be proved in the following section, the simulation can produce qualitative description to the droplet deformation and mass interminglement, which helps understand the experimental observations.

3.2 Numerical Specifications

The schematic of the three-dimensional computational domain and the adaptive mesh for the present VOF simulation are shown in Fig. 4. The domain is in height and in both width and depth. The density and viscosity are and for the liquid, and and for the gas, respectively. The surface tension coefficient of the gas-liquid surface is denoted by σ. The two droplets colliding along the x-direction have zero velocity components in the - and z-directions. Their velocity components in the x-direction are and so that the relative velocity is and the momentum of the entire collision system remains zero. The natural oscillation time of the large droplet is , by which the non-dimensional time can be defined as . The outflow boundary conditions are specified on all the boundaries.

In the present study, the numerical method solves the incompressible and variable-density Navier-Stokes equations with surface-tension, where the density and viscosity in the flow field are varied and constructed by the convective volume fractions of gas and liquid phases while the impressibility is ensured locally. The VOF method adopted by the study has been discussed in great detail in [42, 43] and implemented in the open source code, Gerris, which has been widely used in many multiphase flow problems [23, 40, 44, 45]. The high-fidelity interface-capturing method features the three-dimensional octree adaptive mesh refinement, the geometrical VOF interface reconstruction, the coupled VOF/Level-set height-function curvature estimation, and the continuum-surface-force surface tension formulation.

To resolve not only the droplet interface but also the droplet internal flow, the computational domain is divided into three physical zones, such as the gas, the droplet interior, and the droplet interface. Each zone has its own mesh refinement level R, and the minimum mesh size in each zone is of $O(2^{-R})$. Accordingly, we can use (R_1, R_2, R_3) to describe the refinement levels in all the three zones. A typical simulation run with the mesh refinement (5, 6, 7) results in maximally 5957272 grid points, which is equivalent to about 3.35×10^8 grid points on a uniform mesh and takes about 86 hours of real time for a computational time of $T = 2.0$ on two Intel Xeon E5-2692 processors with 48 cores on Tianhe-2 supercomputer.

3.3 Experimental Validations

To validate the present numerical methods for head-on collision ($B = 0$), the coalescence and reflexive separation of two water droplets of unequal sizes were simulated and compared with Ashgriz and Poo's experiment [28], as shown in Fig. 5. It is noted that the Weber number and Ohnesorge number reported in the experiment are defined based on the smaller droplet and have been converted to on the present definitions as $We = 112$ and $\Delta = 2.0$. Tanguy and Berlemont [46] simulated the experiment by using the Level-set method and based on an estimated $D_S = 400\ \mu m$, leading to $Oh = 4.15 \times 10^{-3}$. However, we could not reproduce the experimental images by using their parameters. After reanalyzing the experimental images, as shown in Fig. 5(a), we found that the exact size ratio is $\Delta = 1.82$ and using $We = 102$ and $Oh = 5.10 \times 10^{-3}$ enabled us to quantitatively reproduce all the collision characteristics. More details about the analysis of the experimental images are given in Supplementary Material.

To examine the grid-dependence of the present simulation, we used three sets of mesh refinement levels, such as (5, 6, 7), (5, 6, 8) and (5, 7, 8), which result in maximally 5719053,

6712558 and 6874396 grid points, respectively. As shown in Fig. 5, these meshes produce almost the same results compared with the experimental images in terms of droplet deformation, internal mixing pattern, and stretching separation. As a balance of computational cost and accuracy, the intermediate level of (5, 6, 8) were used to reproduce all the simulation results in the following sections.

To further validate the present numerical methods for off-center collisions, the coalescence and stretching separation of two identical water droplets [28] with $We = 90, \Delta = 1.0$ and $Oh = 6.89 \times 10^{-3}$ were simulated and shown in Fig. 6. Again, the simulation satisfactorily reproduces the complex three-dimensional droplet deformation and accurately predicts the number of satellite droplets after stretching separation. It is noted that we could not reproduce the experimental results by using $We = 83$ reported in Ref. [28], which might not be accurate due to the uncertainty of droplet sizes in the early experimental measurement. The uncertainty of the Weber numbers is 8%, which is about the same as that of the measured size ratio.

4. Hypergolic ignition by slightly off-center droplet collision

4.1 Phenomenological description of hypergolic ignition

The hypergolic ignition by the slightly off-center collision are phenomenologically described for a representative case of $We = 60.9, \Delta = 1.6$ and $B = 0.3$. The shadowgraph images at selected physical times are shown in Fig. 7(a), which are compared with the head-on case ($B = 0.0$) at the same We and Δ adopted from Zhang *et al.* [20], as shown in Fig. 7(b). The non-dimensional times scaled by using the characteristic oscillation time, fixed at $t_{\mathrm{osc}} = 8.83$ ms, are also given in the figures. Considering that the present problem is not merely surface-tension driven, the characteristic collision time, defined as $t_{\mathrm{ine}} = D_L/U$, is also presented for comparison. The rotation of the merged droplet is indicated by an arrow

pointing from the mass center of the larger WFNA droplet to that of the smaller TMEDA droplet.

Similar to the head-on collision of TMEDA and WFNA droplets, the entire process of the slightly off-center collision at $B = 0.3$ can be divided into five distinct stages. Different reference lengths from 1.0 mm to 2.6 mm were used in the figures for better visualization of these stages.

Stage I (0 ms – about 3.6 ms): droplet coalescence and deformation. The contour of the merged droplet can be clearly seen during this stage, and a slightly dark "tail" behind the WFNA droplet is the fuming. The vaporization is negligible in this stage because the heat release from exothermic liquid-phase chemical reactions is not substantial to intensely vaporize the droplet but only makes its surface blurry. The arrow denoting the mass center vector rotates nearly 90 degrees at 3.6 ms for the off-center collision at $B = 0.3$, while it remains almost unchanged for the head-on collision ($B = 0.0$). In addition, the droplet stretching significantly increase the contact surface of two droplets.

Stage II (about 3.6 ms – about 9 ms): droplet heating and vaporization. The droplet is being heated up from the inside to the surface by the liquid-phase reactions. This is inferred by the observation that the opaque vapor starts to expand as the result of the increasing droplet temperature. The merged droplet keeps rotating and the mass center vector turns nearly 180 degrees at 9 ms, meanwhile the droplet is significantly stretched.

Stage III (about 9 ms – about 24 ms): rapid vaporization and reactions. The droplet shape is almost concealed by the rapid expansion of opaque vapor probably because the droplet is totally heated up and results in more rapid vaporization than that in Stage II. It is seen in Fig. 7 that the dark region (gas vapor) expands over $O(1)$ mm during $O(10)$ ms, and

the vaporization-induced flow velocity is sufficiently small to enforce the validity of the gas flow incompressibility.

Stage IV (about 24 ms – about 29 ms): ignition in gas phase and flame propagation. A bright kernel indicating the over-exposed luminous flame within the opaque area is observed at 24.6 ms for $B = 0.3$ as the occurrence of hypergolic ignition, which is about 6 ms earlier than that for $B = 0.0$. Furthermore, the luminous flame propagates rapidly as illustrated by the expansion of the bright kernel and the simultaneous reduction of the opaque region.

Stage V (after about 29 ms): combustion and flame extinction. When the gaseous species are consumed, a seemingly nonflammable condensed-phase product is left behind and preserves its solid-like appearance until the flame extinction. The same phenomena were observed for head-on droplet collision. The flame propagation velocity is about 0.5 m/s as the bright kernel expands over about 2.6 mm during 5.0 ms, implying again that the compressibility effect is indeed negligible.

4.2 Quantitative analysis of the hypergolic ignition

As expatiated in the previous study [20], the analysis of the grayscale levels of the shadowgraph images can be used to systematically determine the ignition delay time with reduced uncertainty. The opaque vapor (or the luminous flame) area can be evaluated by counting the total pixel numbers N_d (or N_b) with a grayscale level G below (or above) the threshold value of $G_{\text{low}} = 5$ (or $G_{\text{high}} = 250$) in the entire image. The grayscale level of background is set to an intermediate value of $G = 100$. As a result, two time-dependent ratios can be defined as

$$r_d = N_d(t|G < G_{low})/N, \quad r_b = N_b\big(t|G > G_{high}\big)/N \tag{3}$$

where N is the total pixel numbers in the entire image; the subscripts “d” and “b” denote dark and bright.

Figure 8 shows the evolution of the two ratios for the two representative cases discussed in Section 4.1. The division of the entire process being into five stages is substantiated by the greyscale analysis. Specifically, r_d remains a small value in Stage I, experiences an approximately linear increase in Stage II, and shows another approximately linear increase with a larger slope in Stage III. The different change rates of r_d underlie the above division of droplet heating with slow vaporization from the droplet rapid vaporization. Meanwhile, r_b stays at nearly zero in the first three stages because ignition has not occurred. During Stage IV, a rapid decrease of r_d and a sharp increase of r_b happen simultaneously because of the consumption of opaque gaseous species and the expansion of luminous flame. The ignition delay time (IDT) can be therefore defined as the turning point of r_b between Stage III and Stage IV. In Stage V, r_b decreases to its initial value because the propagating flame finally extinguishes after consuming all the gas-phase combustible, while r_d remains as a small constant value because of the opaque non-flammable condensed-phase product. Although the trends of r_d and r_b are similar for $B = 0.3$ and $B = 0.0$, they have significant differences on the time evolution.

First, the time duration of Stage II for $B = 0.3$ (about 7ms) is substantially shorter than that for $B = 0.0$ (about 20 ms), indicating that the merged droplet by slightly off-center collision is easier to be heated up than by the head-on collision. This can be attributed to the enhanced internal mixing by droplet stretching at $B = 0.3$.

Second, the time duration of Stage III for $B = 0.3$ is moderately longer than that for $B = 0.0$. This can be understood by that, on the one hand, to reach the approximately equal peak value of r_d, the amount of opaque vapor at the instant of the commencement of the rapid vaporization for $B = 0.3$ is less than that for $B = 0.0$; on the other hand, the slope of r_d for $B = 0.3$ is smaller because the combustible gaseous mixture has been expanded to a larger area and probably subjected to an increased heat loss.

Third, it is clearly seen from the turning point of r_b that the accurately identified IDT for $B = 0.3$ (24.0 ms) is 6.6 ms shorter than that for $B = 0.0$ (30.6 ms). In Stage IV, the slope of r_d for $B = 0.3$ is smaller than that for $B = 0.0$ because the combustible gaseous species for the former case is spread out in a broader area and is consumed more slowly by the flame.

Overall, compared with the head-on collision, the slightly off-center collision results in faster droplet heating and vaporization, and thereby leading to a shorter IDT. It was hypothesized that this is caused by the enhanced internal mixing by droplet stretching. Consequently, the droplet internal mixing will be discussed in the following section by the use of numerical simulation.

4.3 Mixing enhancement by slightly off-center droplet collision

Figure 9 shows three sets of experimental shadowgraph images and simulation results that were selected and compared at three representative moments, indicated in Fig. 8 by "R" for $B = 0.3$ and "S" for $B = 0.0$. The column (a) is the experimental images amplified for a clearer illustration, in which the droplet surface contours (on the x-z plane) are delineated in red. The columns (b)-(d) are the corresponding simulation results viewed from three different directions, where the red denotes the fluid mass from the TMEDA droplet and the gray the WFNA droplet. The column (e) shows pressure contours and streamlines on the slices cut by the x-z plane. It is reemphasized that the impact velocity is along the x-direction and the droplets deviate from head-on situation in the z-direction, thus the x-z plane is the symmetric plane of the collision system.

The first representative instant, indicated as R1 for $B = 0.3$ and S1 for $B = 0.0$, was selected from their corresponding Stage I. The agreement between the experimental time (2.4 ms) and the computational time (2.2 ms) are very good, substantiating the quantitative prediction of the present simulation on droplet collision dynamics. The slightly off-center

collision causes the merged droplet to rotate and stretch so that the droplet resembles an asymmetric "spoon", while the head-on collision results in an axisymmetric saucer-like droplet shape. The enhanced stretching effects around the contact surface of two droplets can be further verified by the streamline in Fig. 9(e).

The second representative instant, indicated as R2 for $B = 0.3$ and S2 for $B = 0.0$, was selected from their corresponding Stage II. There is a slight discrepancy between the experimental time (7.0 ms) and the computational time (5.0 ms). This is because Stage II involves droplet heating and slight vaporization, the increased droplet surface temperature reduces the surface tension and hence prolongs the droplet oscillation time, $t_{\mathrm{osc}} = \sqrt{\rho_L D_L^3/\sigma_L}$, which is fixed in the present simulation. The direct observation indicates that the mass interminglement at R2 seems stronger than that at S2, because mass is spread out close to the droplet surface in addition to the bulge-like internal mixing pattern emerged in both cases.

The third representative instant R3 for $B = 0.3$ was selected form Stage III, while S3 for $B = 0.0$ was still in Stage II. There is a moderate discrepancy between the experimental time (13.0 ms) and the computational time (7.4 ms) because the droplet is affected by rapid liquid-phase reactions and vaporizations. Considering the mass interminglement during Stage I and Stage II is the controlling mechanism responsible for the non-monotonic ignition delays, the discrepancy does not affect the present conclusions. It is noted that the merged droplet has been completely concealed by the opaque vapor at R3 while it can be seen at S3. The bulge-like internal mixing pattern can still be seen clearly in both cases. For the slightly off-center collision at $B = 0.3$, the evidently intense interminglement of the liquid mass within the merged droplet could lead to a more uniform droplet vaporization. For the head-on collision at $B = 0.0$, as indicated by the streamlines shown in Fig. 9(e), the separation tendency could suppress the mass interminglement between two droplets.

To facilitate the recognition in the first place of the correlation between the mass interminglement and the hypergolic ignition, we added the temporal area changes of the colored contact surface of the droplets to Fig. 8. The contact surface area $A(t)$ of the droplets is normalized by the initial surface area A_0 of the droplets. Because the mesh resolutions on the gas-liquid interface and inside the droplet are the same in the present simulation setup, the normalized colored contact surface area $A(t)/A_0$ can be approximately calculated by

$$\frac{A(t)}{A_0} = \frac{N[0<\phi(t)<1]H[f(t)-1]}{N[0<f(0)<1]} \tag{4}$$

where N is the number of the meshes in which the VOF function $f(t)$ or the mass dye (color) function $\phi(t)$ take certain values, and thus it can be treated as functionals of $f(t)$ or $\phi(t)$. The VOF function $f(t) = 1$ denotes the droplet interior, $0 < f(t) < 1$ the gas-liquid interface, and $f(t) = 0$ the gas; the color function $\phi(t) = 1$ denotes the smaller droplet interior, $0 < \phi(t) < 1$ the contact surface of the droplets, and $\phi(t) = 0$ the larger droplet interior. In the above expression, the Heaviside step function ensures only those meshes within the droplet interior to be counted for calculating the colored contact surface.

As shown in Fig. 8, it should be noted that the lines denoting $A(t)/A_0$ end at the computational time $T = 1.0$, beyond which the simulation cannot accurately capture the droplet mixing significantly influenced by chemical heat release and rapid vaporization, as we have discussed in the Introduction. The results show that the general evolutions of $A(t)/A_0$ and r_d for $B = 0.3$ and $B = 0.0$, respectively, are qualitatively correlated, indicating the mass interminglement for slightly off-center droplet collision is indeed enhanced and critical to the hypergolic ignition.

5. Hypergolic ignition by moderately off-center droplet collision

The shadowgraph images and the grayscale level analysis of the hypergolic ignition by moderately off-center droplet collision at $We = 60.9, \Delta = 1.6$, and $B = 0.6$ are shown in Fig. 10(a) and Fig. 11(a), respectively. Although the five stages similar to the cases discussed in Section 4.1 can be still observed, they display different characteristics.

In Stage I, the droplet stretching at $B = 0.6$ is more substantial compared with the case at $B = 0.3$. In Stage II, a liquid filament is formed with a slight fuming around it, as seen at about 5.4 ms, indicating that the filament contains the mass stretched from the WFNA droplet. After the stretching separation at 6.4 ms, the TMEDA droplet carrying some mass from the WFNA droplet moves away from the WFNA droplet, with a satellite droplet between them and surrounded by large amounts of opaque vapors. It is inferred that the satellite droplet contains both TMEDA and WFNA as a result of mass exchange during the droplet stretching. The satellite droplet disappears to form the gaseous species and some smaller "daughter" droplets at about 20.4ms because of its micro-explosion and eruption.

The ignition occurs at about 32.0 ms as the emergence of a bright kernel. However, the luminous flame only propagates over a small area restricted to in the upper left of the image and extinguishes at about 37.0 ms with a large amount of unburned gaseous species being left. This can be seen by a relatively small value of r_b in Stage IV and a relatively large value of r_d at the end of Stage V in Fig. 11(a). It implies that the unburned gaseous species are not a mixture of TMEDA and WFNA mass but either one of them. Consequently, owing to the insufficient mass participating in the liquid-phase reactions, the case at $B = 0.6$ results in a longer ignition delay time (32.2 ms) compared with the cases at $B = 0.3$ (24.0 ms) and $B = 0.0$ (30.6 ms).

Compared with the cases of head-on or slightly off-center collisions, the most different characteristics for the case at $B = 0.6$ is that there are no distinctly separated slow

and rapid vaporization stages. Instead, an approximately consistent increase of r_d spans over the entire process of vaporization, implying that the droplet heating process is fast. This can be understood as that, the locally formed filament and the satellite droplet have a large surface/volume ratio so that they can be quickly heated up. However, the case at $B = 0.6$ does not develop opaque vapors as much as those in the cases of $B = 0.3$ and $B = 0.0$, because the large portion of droplet mass of each fluid have moved away from the filament and satellite droplet. Consequently, only portions of TMEDA and WFNA participate in the liquid-phase reactions, rendering less heat release and gas-phase species for ignition.

6. Hypergolic ignition by nearly grazing droplet collision

The shadowgraph images and the grayscale level analysis of the hypergolic ignition by nearly grazing droplet collision at $We = 60.9, \Delta = 1.6,$ and $B = 0.9$ are shown in Fig. 10(b) and Fig. 11(b), respectively. Overall, the case at $B = 0.9$ is similar to that of $B = 0.6$ except that it results in more substantial droplet stretching, significantly less amount of mass interminglement, and thereby no hypergolic ignition.

The nearly grazing collision forms a thinner filament that is readily to separate, as shown at 3.0 ms in Fig. 10(b). The locally enhanced mass interminglement in the filament and in the satellite droplet also causes some liquid-phase reactions, as manifested by the opaque vapors. However, the intermingled mass is too little to release a sufficient amount of heat for further droplet vaporization and hypergolic ignition. After the stretching separation, some opaque vapors around the WFNA droplet blur the droplet surface while the surface of the TMEDA droplet remains clear. This can be understood as that, the WFNA droplet grasps some TMEDA mass during the droplet separation, and the exothermic liquid-phase reactions facilitate the WFNA vaporization, which however is insufficient to trigger hypergolic ignition.

These observations are further proved by the grayscale level analysis in Fig. 11(b) that r_d has a slight increase during the entire process while r_b remains nearly zero because no bright ignition kernel is formed.

As another albeit indirect evidence of the varying extent of mass interminglement and liquid-phase reactions with the impact parameter, Fig. 10(c) shows the major condense-phase products at the end of the collision process for the four cases discussed above. The solid-like surface appearance for the slightly off-center droplet collision at $B = 0.3$ resembles that for head-on collision at $B = 0.0$ but looks smoother. For the moderately off-center collision at $B = 0.6$, the product surface is similar to the unreacted droplet but looks turbid possibly because of solid-phase products suspended in the incompletely reacted droplet. The product for the nearly grazing collision at $B = 0.9$ is an almost unreacted droplet which holds the smooth surface appearance.

Overall, as the normalized contact surface area of the droplets illustrated in Fig. 8 and Fig. 11, the results show that the general evolutions of $A(t)/A_0$ and r_d are qualitatively correlated so that they show the same non-monotonic variation with varying impact parameters. This partially indicates that the mass interminglement in the early stage of droplet collision is critical to the subsequent liquid-phase reactions, droplet vaporization and hypergolic ignition. However, we note that $A(t)/A_0$ is a rough quantification of the mass interminglement and more rigorous discussions about the correlation between the mass interminglement and the IDT are given in the following section by use of the precisely defined "mixing index".

7. Correlation between mass interminglement and IDT

Based on the discussions in the preceding sections, a non-monotonic variation of IDT with increasing the impact parameter is qualitatively correlated with the varying degree of mass interminglement. As can be further seen in Fig 12(a), the VOF simulations for five cases at fixed $We = 60.9$ and $\Delta = 1.6$ but varying B from 0.0 to 0.9, supplement the experimental shadowgraph images by providing useful information about the internal flow and mass interminglement of droplet. It is clearly seen that, the droplet mass is increasingly intermingled with increasing B from 0.0 to 0.3, where the droplet remains coalesced. This enhanced mass interminglement can be attributed to the better droplet mixing and the shorter IDT at $B = 0.3$. Further increasing B to 0.6 and higher values, the droplet stretching deformation becomes more intense but the coalesced droplet eventually separates into two major masses with a certain number of satellite droplets. Although the enhanced mass interminglement facilitate droplet mixing and hence liquid-phase reactions, the amount of mass participating in the reactions is however reduced due to the droplet separation. This explains the elongation of IDT at $B = 0.6$ compared with that at $B = 0.3$, and the non-ignitability of the system at $B = 0.9$.

For a quantitative correlation between the IDTs and the mass interminglement, a time-dependent "mixing index" [23, 47], $M \in [0,1]$, whose variants have been proposed and used in previous studies [23, 48], was adopted by the present study. The index can be defined by

$$M = 1 - \frac{\int_V |C - C_\infty| H(f-1) \mathrm{d}V}{\int_V |C_0 - C_\infty| H(f-1) \mathrm{d}V} \tag{5}$$

Where f is the spatially and temporally VOF function with $f = 1$ in droplet interior, $f = 0$ in gas, and $0 < f < 1$ on the droplet interface; $H(f-1)$ is the Heaviside step function restraining the volumetric integrations within the droplets. C is the spatially and temporally varying "concentration" function measuring the degree of "mixing", or more rigorously, mass interminglement. C_0 and C_∞ are the "concentrations" defined in the initially unmixed

droplets and for an ideal situation of "well-mixing", respectively. These "concentration" functions are defined by

$$C_0 = \begin{Bmatrix} 0, & \phi = 0 \\ 1, & \phi > 0 \end{Bmatrix}, C_\infty = 1/(1+\Delta^3)\,, C = \frac{|\phi - 0.5|}{0.5} C_0 \tag{6}$$

where ϕ is the mass dye function with $\phi = 1$ in the smaller droplet, as seen by the red dye in Fig. 12(a), and $\phi = 0$ otherwise.

The "mixing indices" for the five cases of Fig. 12(a) are shown in Fig. 12(b) for comparison. It is seen that M for $B = 0.3$ is larger than that for $B = 0.0$ during almost the entire collision process except in the early stage between R1(or S1) and R2(or S2), when the coalesced droplet has reached the maximum deformation and starts to contract under surface tension. This demonstrates that the mass interminglement and therefore the droplet mixing and liquid-phase reactions are indeed enhanced by slightly off-center collision at $B = 0.3$.

For the moderately off-center droplet collision at $B = 0.6$, the rapid increase of M during the early stages attributes to the formed filament and satellite droplets, where mass interminglement is enhanced. However, the increase of M becomes slower in the later stages because of the occurrence of stretching separation suppresses the further mass interminglement, as seen in Fig. 12(a) the large portion of the larger droplet remaining intact. Consequently, the IDT for $B = 0.6$ becomes larger than that for $B = 0.3$ because a smaller amount of liquid mass participates in the exothermic liquid-phase reactions and thereby the droplet requires a longer time to produce sufficient gas-phase species for ignition.

The additional case at $B = 0.7$ was added to show the transition to the nearly grazing droplet collision at $B = 0.9$. The "mixing index" for the case at $B = 0.7$ is almost the same with that for the case at $B = 0.6$ in the early stages, but it only slightly increases in the late stages, resulting evidently smaller M. As discussed above, the stretching separation occurs

increasingly earlier with increasing B, and a decreasing amount of mass participates in the following interminglement and mixing. This trend is more notable for the case at $B = 0.9$, where M remains almost a small constant after the initial increase for a short period of time.

Although Fig. 12 shows the correlation between the non-monotonic variations of M and IDT with increasing the impact parameters, we noted some discrepancies between the experimental and simulation results about the droplet deformation, especially for the moderately off-center collisions at $B = 0.6$ and 0.7 involving filament separation. The underlying reason is that the local physical properties of the locally formed filament, such as viscosity and surface tension, might have been changed because of the chemical heat release from the liquid-phase reactions. Although such a local variation of physical properties would not be significant for the whole droplet, but it can substantially change the subsequent fluid dynamics of the thin filament, particularly its separation tendency. Regardless of the deficiency of the present simulation in predicting the filament separation and the number of resulting satellite droplets, which is a challenging task even for non-reacting, isothermal droplet collision, the controlling physics of the mass interminglement is correctly captured by the simulation.

8. Parametric study on hypergolic ignitability and IDT

As per the scope of the present study discussed in Section 3, three controlling non-dimensional parameters, namely, We, Δ and B, were considered in the parametric study. It is noted that the effects of We and Δ on the head-on collision ($B = 0$) between TMEDA and WFNA droplets have been investigated in detail in the previous study [20]. Consequently, the present study was focused on elucidating the effects of B at various Wes and Δs. In order to quantify the effects of B on the hypergolic ignitability, a large number of experiments have

been systematically conducted and presented in the $We - B$ parameter space for two typical size ratios $\Delta = 1.6$ and $\Delta = 2.0$, as shown in Fig. 13.

For $\Delta = 1.6$, an approximately straight line, fitted as $B = -0.0005We + 0.75$, separates the $We - B$ subspace composed of $We \in [20,140]$ and $B \in [0.0,1.0]$ into two regimes: the ignitable regime below the line and the non-ignitable regime above it, as shown in Fig. 13(a). The negative slope of the fitted regime boundary line indicates that increasing We at a certain large value of B tends to result in non-ignitability. This result is different from that obtained from the regime nomogram in the $We - \Delta$ parameter space for head-on droplet collision [20], where the hypergolic ignitability favors small Δ (for appropriate fuel/oxidizer ratio favored by the reaction TMEDA + $2HNO_3$ → TMEDADN) and large We. Increasing We for head-on droplet collision promotes the droplet mixing and reactions but increasing We for off-center collision with large B weakens the droplet mixing and reactions by the stretching separation.

For $\Delta = 2.0$, two approximately straight lines, fitted as $B = -0.0018We + 0.75$ and $B = -0.01We + 0.8$, separate the parameter subspace into three regimes, as shown in Fig. 13(b). The upper non-ignitable regime can be explained by the same reasons stated above for the case of $\Delta = 1.6$. The emergence of the lower non-ignitable regime is mainly because the larger size ratio makes the system to deviate from the appropriate fuel/oxidizer ratio. At small B and small We, the ignitability of the system is similar to that of the head-on case. Increasing B for droplet stretching deformation helps create an appropriate fuel/oxidizer ratio in the filament and the satellite droplet; increasing We promotes the mass interminglement. The synergetic effects of increasing B and We moves the system from the lower non-ignitable regime to the ignitable regime.

The non-monotonic variation of IDT with B has been expatiated in the preceding sections for the representative case at $We = 60.9$ and $\Delta = 1.6$. By the use of the present parametric study, the non-monotonicity is further confirmed for other Wes and Δs, as shown in Fig. 14. Specifically, Fig. 14(a) and Fig. 14(c) present the cases with $We = 41.0$ and $We = 83.0$, respectively; Fig. 14(b) presents the cases at $We = 60.9$ but with different size ratios, such as $\Delta = 1.3$ and $\Delta = 2.0$.

The results show that the non-monotonic variation of IDT with increasing B from 0.0 to 0.7 is a general characteristic of the present hypergolic system, which can be observed for most combinations of (We, Δ, B). For example, for Δ =1.3 and 1.6, the IDT first decreases and then increases as increasing B, although the value of B corresponding to the minimum IDT slightly varies with We. It is also noted that at $\Delta = 2.0$ and small Weber numbers, such as $We = 41.0$ and 60.9, the IDT decreases monotonically as increasing B from 0.2 to 0.6. This can be understood by that the large size ratio of 2.0 reduces the ignitability of the hypergolic system by deviating the system from the chemical stoichiometry of the liquid-phase reactions; but a larger B leads to the substantial stretching separation, the less mass interminglement, and more appropriate fuel/oxidizer ratio, so that the ignitability is enhanced. However, the non-monotonicity can be observed again when We increases to 83.0. This is because, although increasing We can generally enhance the droplet mixing in head-on or slightly off-center collisions, it reduces the characteristic time for mass interminglement during droplet stretching and therefore makes the IDT to increase again.

9. Concluding Remarks

In the previous study on the hypergolic ignition of the head-on collision between a smaller TMEDA and a larger WFNA droplet at various Wes and Δs [20], the ignitability and

IDT critically rely on the heat release from the liquid-phase reactions, which in turn is determined by the effective droplet internal mixing during earlier stages. The present study has extended our understanding from the rare event of head-on collision to more frequently seen off-center collision, as summarized in the following.

The impact parameter effects on IDT were first studied for a representative case at $We = 60.9, \Delta = 1.6$ and $Oh = 2.5 \times 10^{-3}$. Compared with the head-on collision, the IDT for the slightly off-center collision is shorter because of the promoted mass interminglement owing to the enhanced droplet stretching deformation, which is characterized by the formation of thin liquid filament. However, the filament tends to break up with increasing B, resulting in a smaller amount of liquid mass participating in the liquid-phase reactions, less vaporized gas-phase species, and prolonged ignition delay (for moderately off-center collision) or even non-ignitability (for nearly grazing collision).

The non-monotonic influences of B on the hypergolic ignition can be correlated with the non-monotonic effects of B on the mass interminglement of colliding droplets. Specifically, for slightly off-center collision, the droplet stretching leads to the more intense interminglement of the liquid mass within the merged droplet, which is computationally verified by evident mass spreading out close to the droplet surface in addition to the bulge-like internal mixing pattern. To further increase B, the substantial stretching effect results in stretching separation, which suppresses the mass interminglement between the droplets. Consequently, only portions of TMEDA and WFNA mass participate in the liquid-phase reactions, rendering less heat release and gas-phase species for ignition. The correlation between the mass interminglement and IDT has been quantitatively verified by examining the defined mixing index.

A systematic study on the ignitability and IDT has been conducted for $We = 20 - 140$ and $\Delta = 1.3 - 2.0$ but at the fixed $Oh = 2.5 \times 10^{-3}$. The ignitability nomogram in

$We - B$ parameter subspace shows that, for off-center collision at small B, the ignitability of the system is enhanced as increasing We, which is similar to that of the head-on collision; for off-center collision with large B, the ignitability of the system is suppressed as increasing We and B because of the suppressed mass interminglement by the stretching separation. The non-monotonic variation of IDT with varying B has been also confirmed for more Wes and Δs, showing the non-monotonicity is a general characteristic of the present hypergolic system.

Future experimental studies can be to study the effects of Ohnesorge number (or more generally, the size effect) and higher Weber numbers. Although the present simulation captured the important physics of droplet mass interminglement that is crucial to the subsequent droplet behaviors, the simulation cannot capture the entire hypergolic ignition process due to the lack in heating and reactions. These absent physical effects should be accounted for in our future studies, including the transport phenomena and chemical reactions in the present VOF simulation. Furthermore, for applications in real engines, the collisions between two impinging jets [15, 16, 41, 49-51] are of significance. However, it is recognized that, unless the mesh resolution is sufficiently high, those simulations of jets and sprays cannot correctly reflect droplet collision events, which occur at much smaller length scales than the jets (sprays) and whose physical description requires physics at even smaller scales. Subgrid modelling for droplet collisions is needed in the simulation of jets and sprays. This can partially explain the constant research interests in droplet collision over decades.

Acknowledgement

The work was supported by NSFC (51722603 and 91641105), the Hong Kong Research Grants Council/General Research Fund (PolyU 152217/14E and PolyU 152651/16E), and Central Research Grant (G-YBXN) of the Hong Kong Polytechnic University.

Reference

[1] S.M. Davis, N. Yilmaz, Advances in hypergolic propellants: Ignition, hydrazine, and hydrogen peroxide research, Adv. Aerosp. Eng. 2014 (2014).

[2] E.A. Fletcher, G. Morrell, Ignition in liquid propellant rocket engines, in: M.G. J. Ducerme, A. H. Lefebvre (Ed.), Progress in Combustion Science and Technology Volume I, Pergamon, Oxford. London. New York. Paris, (1960)183-215.

[3] E.A. Hurlbert, R.J. Moreland, S. Candel. Propellant ignition and flame propagation. 2nd Int. Symp. on Liq. Rocket Propul., Chatillon, (1995)13.11-13.20.

[4] G.P. Sutton, O. Biblarz, Rocket propulsion elements, 8ed., John Wiley & Sons, Hoboken, New Jersey, 2010.

[5] M. Kilpatrick, L.L. Baker. A study of fast reactions in fuel-oxidant systems: Anhydrous hydrazine with 100 per cent nitric acid, Symp. (Int.) Combust (1955) 196-205.

[6] D. Erik, C. Kevin, P. Timothée, H. Stephen, Ignition of Advanced Hypergolic Propellants, 46th AIAA/ASME/SAE/ASEE Joint Propulsion Conference & Exhibit, AIAA (2010) 6984.

[7] S. Wang, S.T. Thynell, A. Chowdhury, Experimental study on hypergolic interaction between N, N, N′, N′-tetramethylethylenediamine and nitric acid, Energy Fuels 24 (2010) 5320-5330.

[8] S. Wang, S. Thynell, An experimental study on the hypergolic interaction between monomethylhydrazine and nitric acid, Combust. Flame 159 (2012) 438-447.

[9] E.M. Dambach, Y. Solomon, S.D. Heister, T.L. Pourpoint, Investigation into the Hypergolic Ignition Process Initiated by Low Weber Number Collisions, J. Propul. Power 29 (2013) 331-338.

[10] C.D. McKinney Jr, M. Kilpatrick, An Apparatus for Measuring the Rates of Some Rapid Reactions, Reactions, Rev. Sci. Instrum. 22 (1951) 590-597.

[11] R.L. Schalla, E.A. Pletcher. The behavior of the system triethylamine—White fuming nitric acid under conditions of rapid mixing, Symp. (Int.) Combust, (1957) 911-917.

[12] M. Kilpatrick, L.L. Baker Jr. A study of fast reactions in fuel-oxidant systems: Anhydrous hydrazine with 100 per cent nitric acid, Symp. (Int.) Combust, (1955) 196-205.

[13] R.L. Schalla, The ignition behavior of various amines with white fuming nitric acid, ARS J. 29 (1959) 33-39.

[14] J.D. Dennis, T.D. Kubal, O. Campanella, S.F. Son, T.L. Pourpoint, Rheological characterization of monomethylhydrazine gels, J. Propul. Power 29 (2013) 313-320.

[15] J.D. Dennis, T.L. Pourpoint, S.F. Son, Ignition of gelled monomethylhydrazine and red fuming nitric acid in an impinging jet apparatus, 47th AIAA/ASME/SAE/ASEE Joint Propulsion Conference & Exhibit, Joint Propulsion Conferences, California, 2011.

[16] J.D. Dennis, S.F. Son, T.L. Pourpoint. Critical ignition criteria for monomethylhydrazine and red fuming nitric acid in an impinging jet apparatus, 48th AIAA/ASME/SAE/ASEE Joint Propulsion Conference & Exhibit, (2012) 4325.

[17] J.M. Forness, T.L. Pourpoint, S.D. Heister. Experimental Study of Impingement and Reaction of Hypergolic Droplets, 49th AIAA/ASME/SAE/ASEE Joint Propulsion Conference, (2013) 3772.

[18] E.M. Dambach, B.A. Rankin, T.L. Pourpoint, S.D. Heister, Temperature estimations in the near-flame field resulting from hypergolic ignition using thin filament pyrometry, Combust. Sci. Technol. 184 (2012) 205-223.

[19] E.M. Dambach, Y. Solomon, S.D. Heister, T.L. Pourpoint, Investigation into the Hypergolic Ignition Process Initiated by Low Weber Number Collisions, J. Propul. Power 29 (2013) 331-338.

[20] D. Zhang, P. Zhang, Y. Yuan, T. Zhang, Hypergolic ignition by head-on collision of N, N, N′ , N′ − tetramethylethylenediamine and white fuming nitric acid droplets, Combust. Flame 173 (2016) 276-287.
[21] J.D. Dennis, T.L. Pourpoint, S.F. Son, Ignition of Gelled Monomethylhydrazine and Red Fuming Nitric Acid in an Impinging Jet Apparatus, 47th AIAA/ASME/SAE/ASEE Joint Propulsion Conference & Exhibit, Joint Propulsion Conferences, California, 2011.
[22] C.K. Law, Fuel options for next-generation chemical propulsion, AIAA J., 50 (2012) 19-36.
[23] C. Tang, J. Zhao, P. Zhang, C.K. Law, Z. Huang, Dynamics of internal jets in the merging of two droplets of unequal sizes, J. Fluid Mech. 795 (2016) 671-689.
[24] M. Orme, Experiments on droplet collisions, bounce, coalescence and disruption, Prog. Energy Combust. Sci. 23 (1997) 65-79.
[25] G. Brenn, Droplet collision, in: N. Ashgriz (Ed), Handbook of Atomization and Sprays, Springer (2011) 157-181.
[26] Y. Jiang, A. Umemura, C. Law, An experimental investigation on the collision behaviour of hydrocarbon droplets, J. Fluid Mech. 234 (1992) 171-190.
[27] J. Qian, C. Law, Regimes of coalescence and separation in droplet collision, J. Fluid Mech. 331 (1997) 59-80.
[28] N. Ashgriz, J. Poo, Coalescence and separation in binary collisions of liquid drops, J. Fluid Mech. 221 (1990) 183-204.
[29] C. Tang, P. Zhang, C.K. Law, Bouncing, coalescence, and separation in head-on collision of unequal-size droplets, Phys. Fluids 24 (2012) 022101.
[30] D. Liu, P. Zhang, C.K. Law, Y. Guo, Collision dynamics and mixing of unequal-size droplets, Int. J. Heat and Mass Transfer 57 (2013) 421-428.
[31] C. Focke, D. Bothe, Computational analysis of binary collisions of shear-thinning droplets, Journal of Non-Newtonian Fluid Mechanics 166 (2011) 799-810.
[32] C. Focke, D. Bothe, Direct numerical simulation of binary off-center collisions of shear thinning droplets at high Weber numbers, Phys. Fluids 24 (2012) 59-80.
[33] K. Sun, T. Wang, P. Zhang, C.K. Law, Non-Newtonian flow effects on the coalescence and mixing of initially stationary droplets of shear-thinning fluids, Phys. Rev. E 91 (2015) 023009.
[34] K. Sun, P. Zhang, C.K. Law, T. Wang, Collision dynamics and internal mixing of droplets of non-Newtonian liquids, Phys. Rev. Appl. 4 (2015) 054013.
[35] F. Blanchette, Simulation of mixing within drops due to surface tension variations, Phys. Rev. Lett. 105 (2010) 074501.
[36] K.-L. Pan, Y.-H. Tseng, J.-C. Chen, K.-L. Huang, C.-H. Wang, M.-C. Lai, Controlling droplet bouncing and coalescence with surfactant, J. Fluid Mech. 799 (2016) 603-636.
[37] T. Inamuro, S. Tajima, F. Ogino, Lattice Boltzmann simulation of droplet collision dynamics, Int. J. Heat and Mass Transfer 47 (2004) 4649-4657.
[38] B. Sakakibara, T. Inamuro, Lattice Boltzmann simulation of collision dynamics of two unequal-size droplets, Int. J. Heat and Mass Transfer 51 (2008) 3207-3216.
[39] Z. Sun, G. Xi, X. Chen, Mechanism study of deformation and mass transfer for binary droplet collisions with particle method, Phys. Fluids 21 (2009) 032106.
[40] X. Chen, D. Ma, P. Khare, V. Yang. Energy and mass transfer during binary droplet collision, 49th AIAA Aerospace Sciences Meeting Including the New Horizons Forum and Aerospace Exposition, Florida, (2011)771.
[41] M. James, T. Kubal, S. Son, W. Anderson, T. Pourpoint. Calibration of an impinging jet injector suitable for liquid and gelled hypergolic propellants, 45th AIAA/ASME/SAE/ASEE Joint Propulsion Conference & Exhibit (2009) 4882.

[42] S. Popinet, Gerris: a tree-based adaptive solver for the incompressible Euler equations in complex geometries, J. Comput. Phys. 190 (2003) 572-600.
[43] S. Popinet, An accurate adaptive solver for surface-tension-driven interfacial flows, J. Comput. Phys. 228 (2009) 5838-5866.
[44] X. Chen, V. Yang, Thickness-based adaptive mesh refinement methods for multi-phase flow simulations with thin regions, J. Comput. Phys. 269 (2014) 22-39.
[45] S. Popinet, Numerical Models of Surface Tension, Annu. Rev. Fluid Mech. 50 2018 1-28.
[46] S. Tanguy, A. Berlemont, Application of a level set method for simulation of droplet collisions, Int. J. Multiphase Flow 31 (2005) 1015-1035.
[47] S.-I. Yeh, W.-F. Fang, H.-J. Sheen, J.-T. Yang, Droplets coalescence and mixing with identical and distinct surface tension on a wettability gradient surface, Microfluid. Nanofluid. 14 (2013) 785-795.
[48] X. Xia, C. He, D. Yu, J. Zhao, P. Zhang, Vortex-ring-induced internal mixing upon the coalescence of initially stationary droplets, Phys. Rev. Fluids 2 (2017) 113607.
[49] N. Bremond, E. Villermaux, Atomization by jet impact, J. Fluid Mech. 549 (2006) 273-306.
[50] X. Chen, D. Ma, V. Yang, S. Popinet, High-fidelity simulations of impinging jet atomization, Atomization Spray. 23 (2013) 1079-1101.
[51] S. Jung, S.D. Hoath, G.D. Martin, I.M. Hutchings, Atomization patterns produced by the oblique collision of two Newtonian liquid jets, Phys. Fluids 22 (2010) 042101.

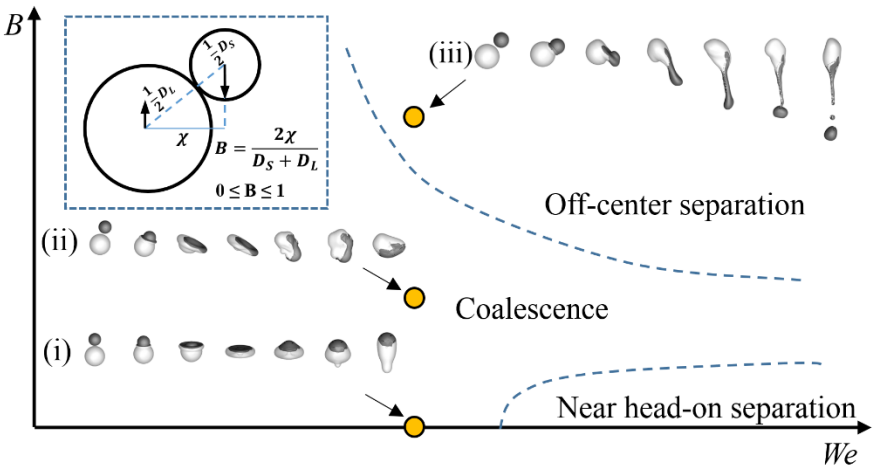

Figure 1. Schematic of droplet collision regimes in the $We - B$ parameter space: (i) head-on coalescence, (ii) off-center coalescence, and (iii) off-center separation. Droplet bouncing occuring at smaller Wes and droplet splashing at higher Wes are not shown for clarity.

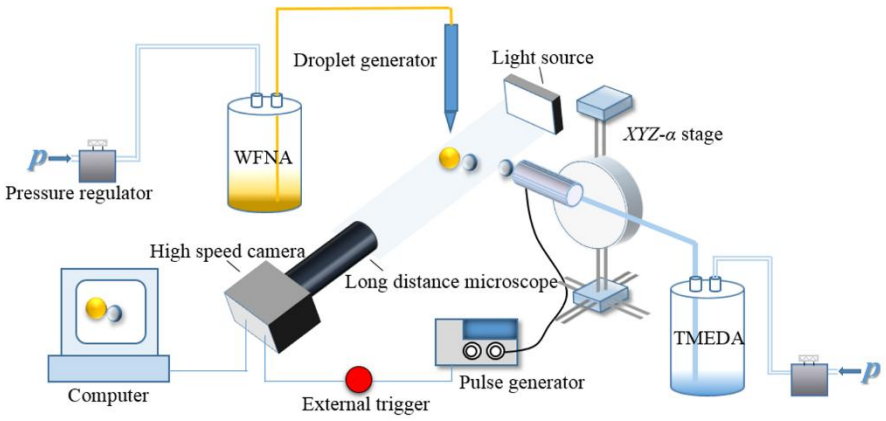

Figure 2. Schematic of the experimental apparatus for hypergolic ignition by binary collision of TMEDA and WFNA droplets.

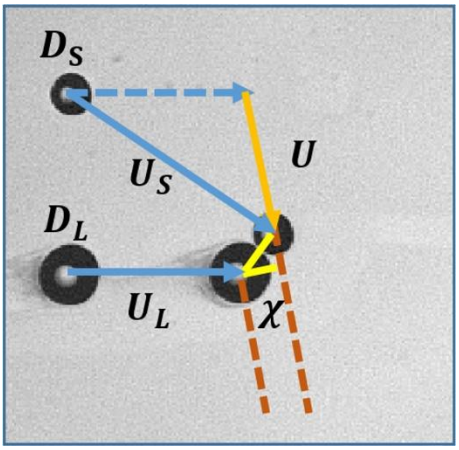

Figure 3. Determination of droplet sizes, velocities and impact parameter based on the time-resolved shadowgraph images.

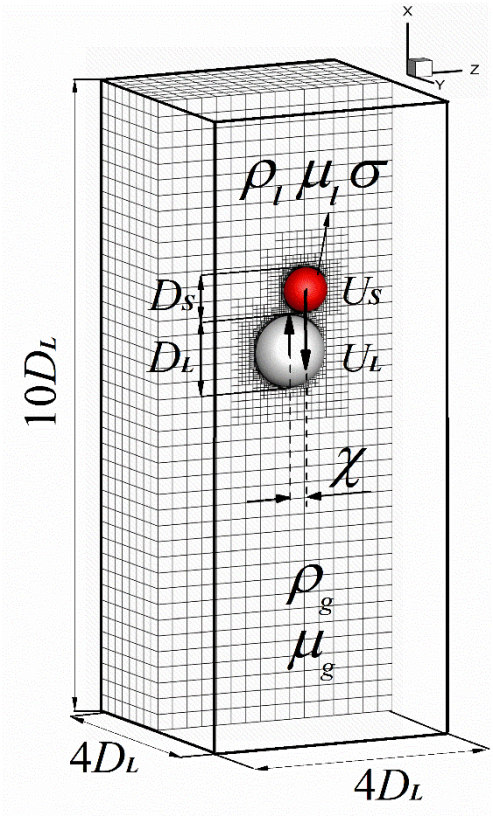

Figure 4. Schematic of the three-dimensional computational domain and the adaptive mesh for the VOF simulation.

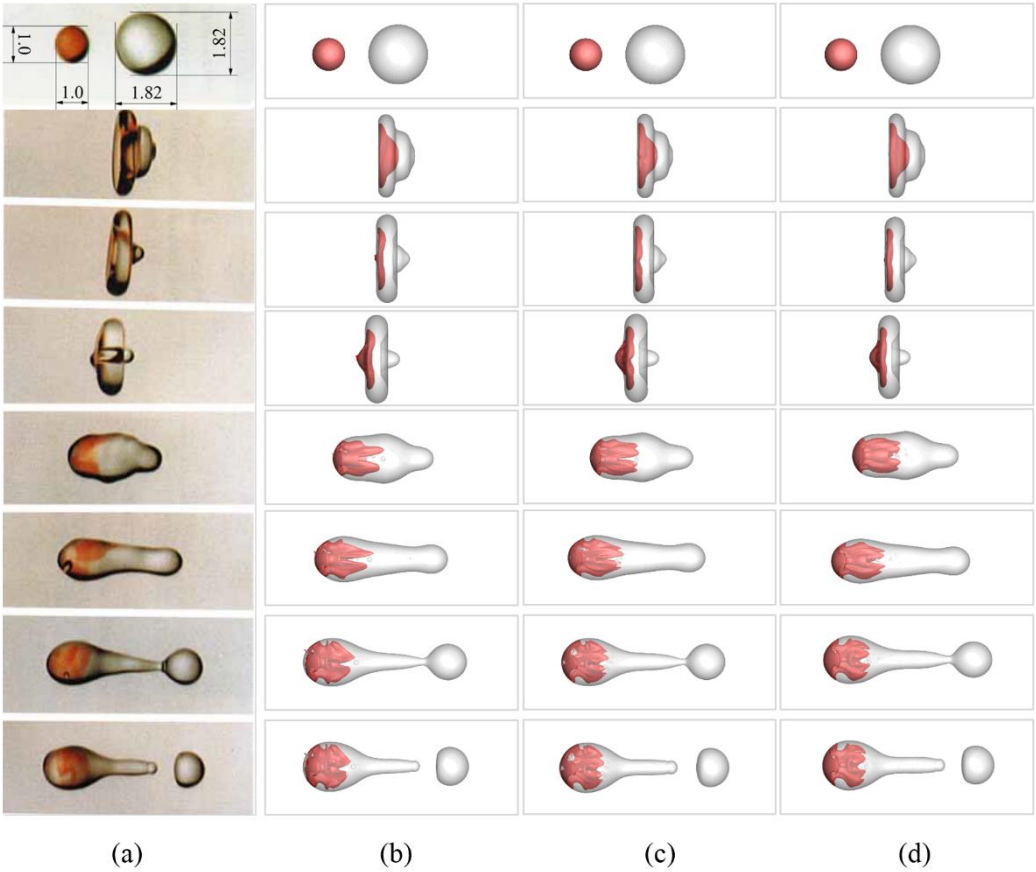

Figure 5. Experimental validation and grid independence analysis of the head-on collision ($B = 0$) of unequal-size water droplets at $We = 102, \Delta = 1.82$ and $Oh = 5.10 \times 10^{-3}$ [26]. (a) Ashgriz and Poo's experiment [26], and three sets of mesh refinement levels with (b) (5, 6, 7), (c) (5, 6, 8) and (d) (5, 7, 8), respectively.

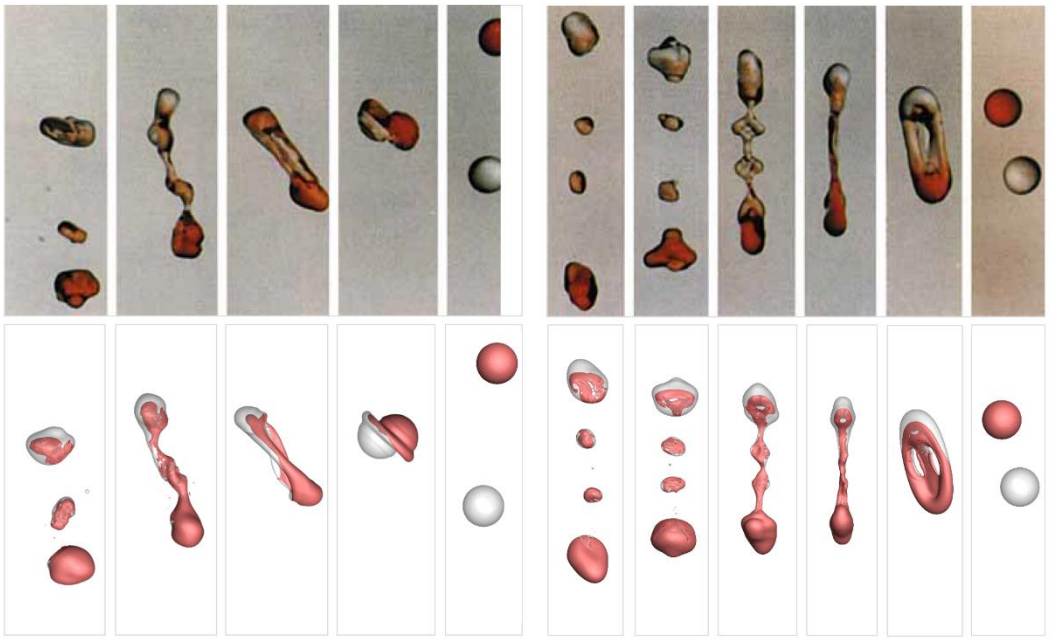

(a) (b)

Figure 6. Experimental validation of the off-center collision of identical water droplets with (a) one satellite droplet at $We = 90$ and $B = 0.34$ and (b) two satellite droplets at $We = 90$ and $B = 0.43$ [26].

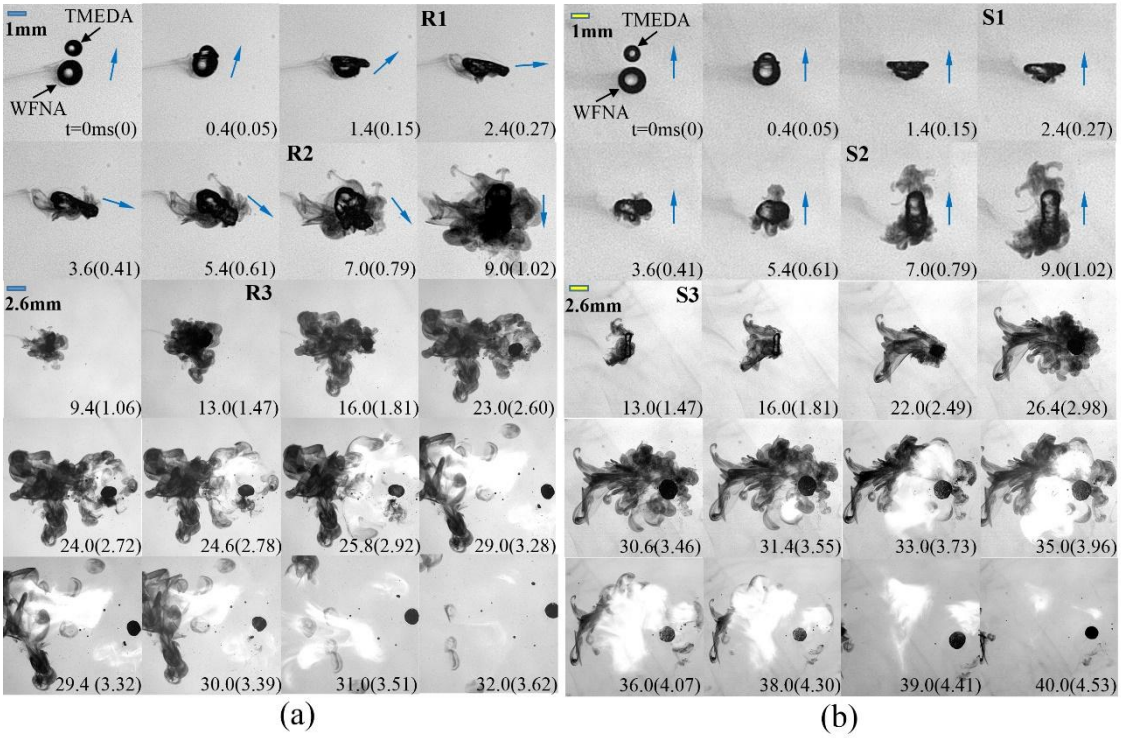

Figure 7. Shadowgraph images of the hypergolic ignition at selected times for two representative cases with the same $We = 60.9$, $\Delta = 1.6$, but different (a) $B = 0.3$ and (b) $B = 0.0$ (adapted from Zhang *et al.* [20]). $t_{\mathrm{ine}} = 1.19\ ms$ and $t_{\mathrm{osc}} = 8.83\ ms$.

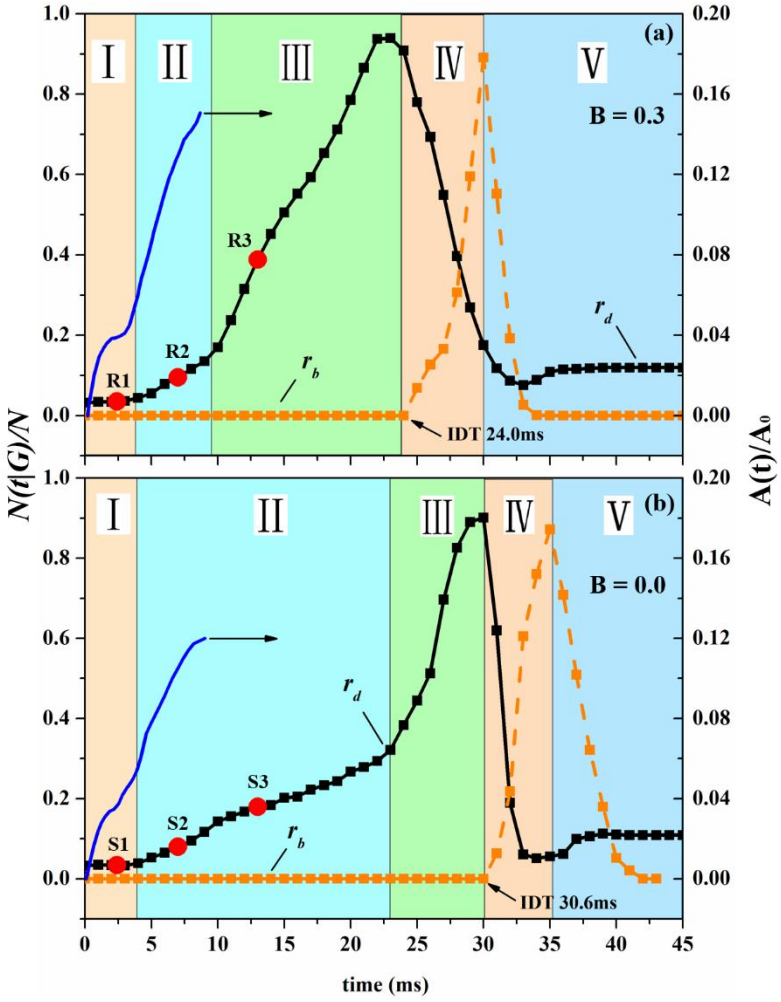

Figure 8. Evolution of $r_d = N_d(t|G < G_{low})/N$, $r_b = N_b(t|G > G_{high})/N$, and normalized contact surface area $A(t)/A_0$ for the two representative cases shown in Fig. 7, (a) B = 0.3 and (b) B= 0.0.

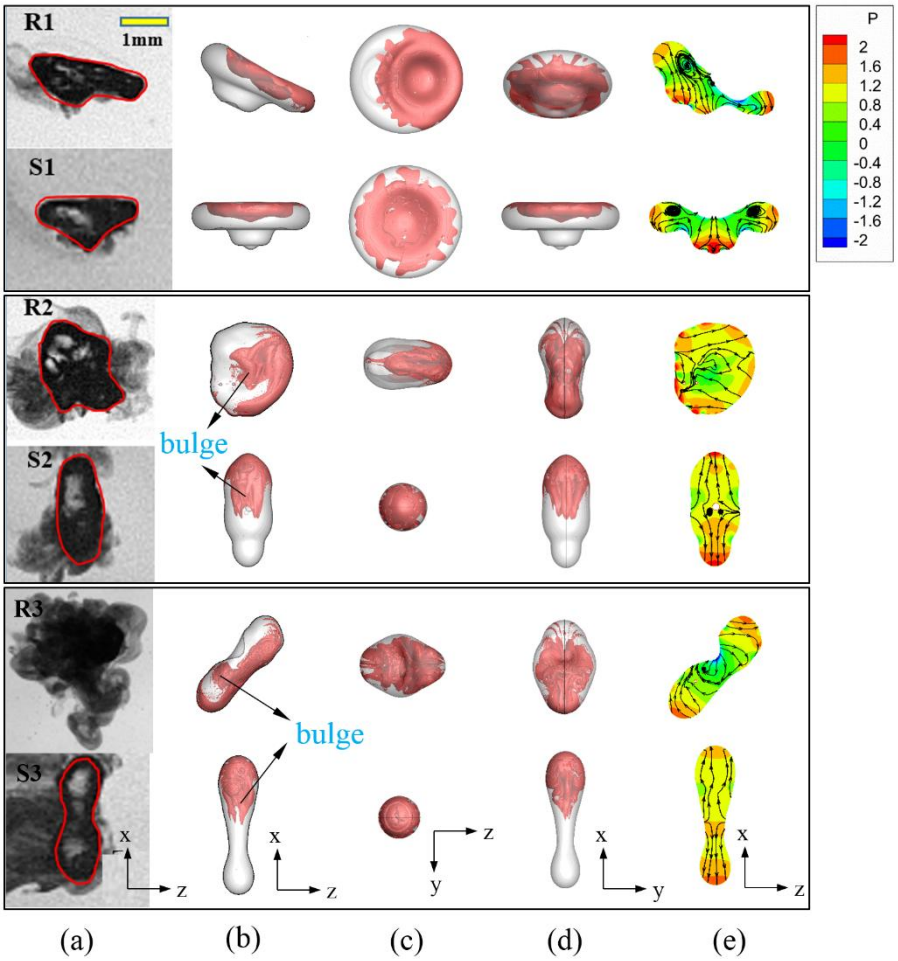

Figure 9. Comparison between $B = 0.3$ (denoted by "R") and $B = 0.0$ (denoted by "S") for three representative moments indicated in Fig. 8. (a) the experimental shadowgraph images, (b)-(d) the simulation results viewed from three different directions, and (e) the pressure contours and streamlines. The experimental times are 2.4ms, 7.0ms, and 13ms, respectively; the computational time T are 0.25, 0.57, and 0.84, respectively, corresponding to the physical times ($t = T * t_{\mathrm{osc}}$) that are 2.2ms, 5.0ms, and 7.4ms, respectively. $t_{\mathrm{osc}} = 8.83\ ms$.

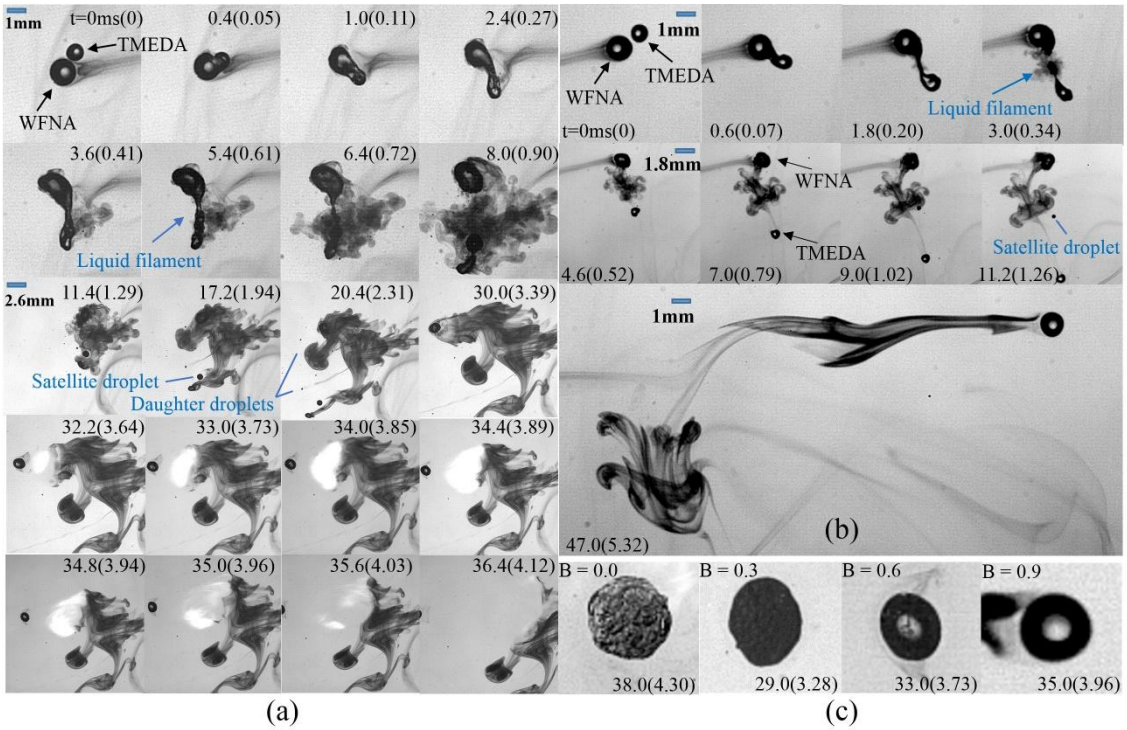

Figure 10. Shadowgraph images of the hypergolic ignition at selected times for two representative cases with the same $We = 60.9$, $\Delta = 1.6$, but different (a) $B = 0.6$ and (b) $B = 0.9$. $t_{\text{ine}} = 1.19\ ms$, $t_{\text{osc}} = 8.83\ ms$; and (c) the surface appearance of the major remaining products at various Bs.

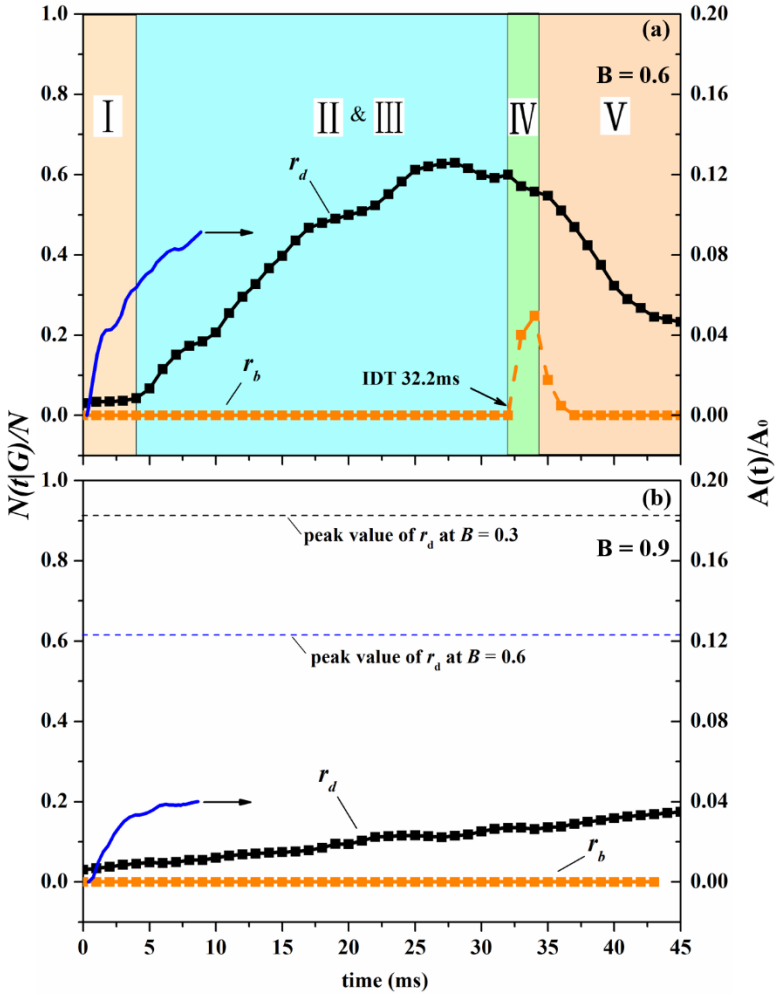

Figure 11. Evolution of $r_d = N_d(t|G < G_{low})/N$, $r_b = N_b(t|G > G_{high})/N$, and normalized contact surface area $A(t)/A_0$ for the representative two cases shown in Fig. 10, (a) B = 0.6 and (b) B= 0.9.

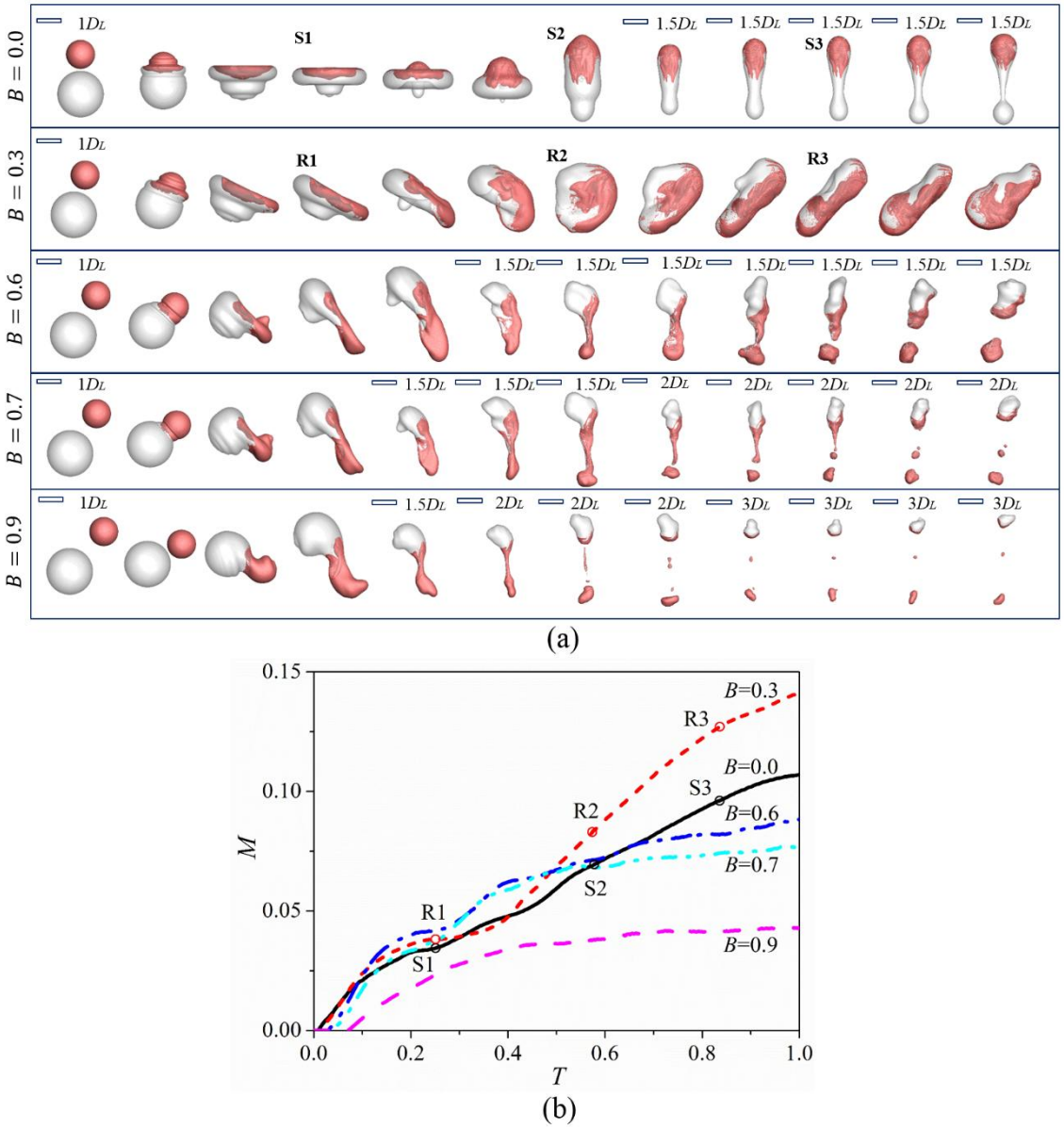

Figure 12. Variation of (a) droplet collision outcomes and (b) mixing index for various impact parameters with $B = 0.0, 0.3, 0.6, 0.7$ and 0.9 at $We = 60.9$ and $\Delta = 1.6$.

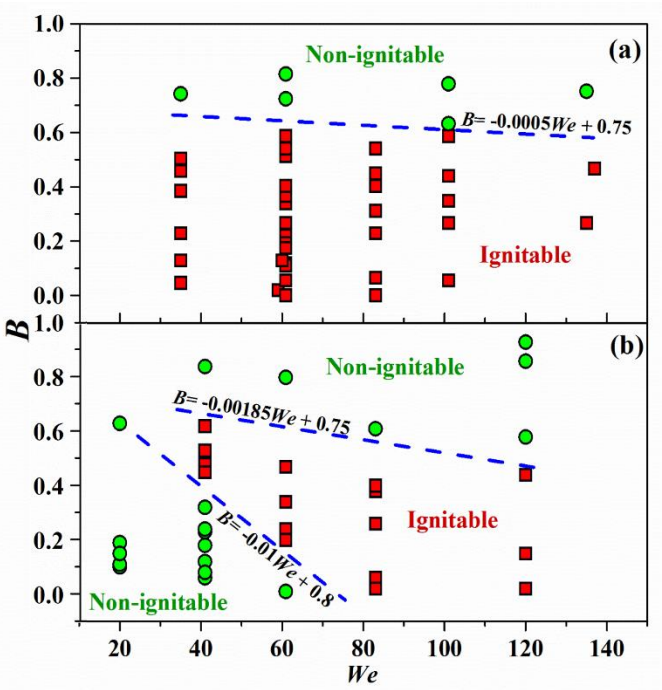

Figure 13. Ignitability regime nomogram in $We - B$ parameter space for (a) $\Delta = 1.6$ and (b) $\Delta = 2.0$.

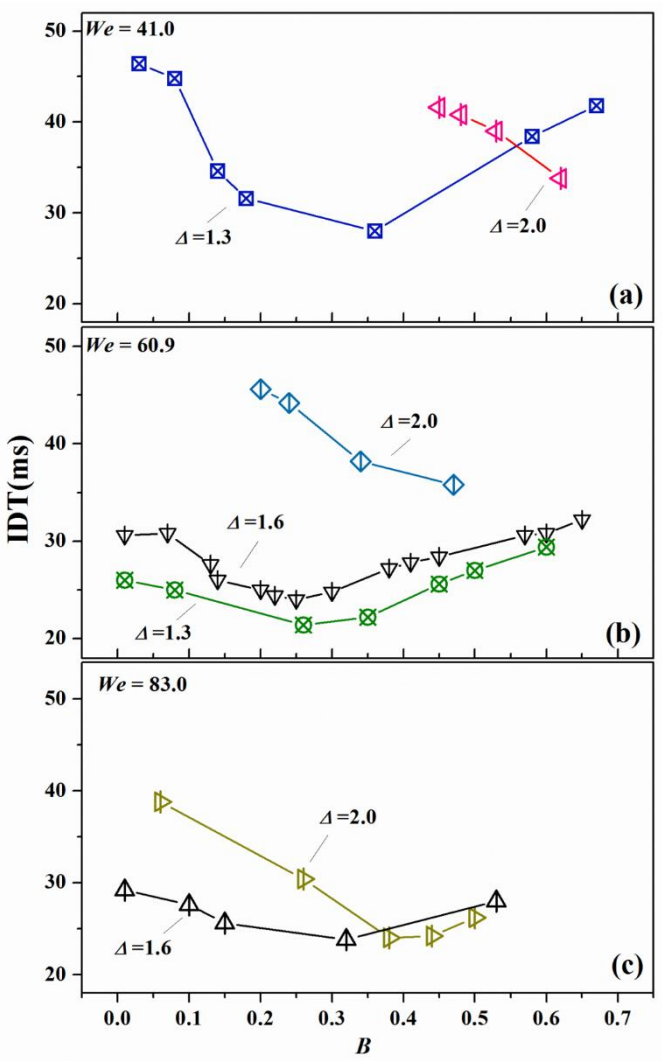

Figure 14. Dependence of IDT on impact parameter, B, for (a) $We = 41.0, \Delta = 1.3$ and $\Delta = 2.0$; (b) $We = 60.9, \Delta = 1.3, 1.6$ and $\Delta = 2.0$; and (c) $We = 83.0, \Delta = 1.6$ and $\Delta = 2.0$.

Figure 1

Click here to download high resolution image

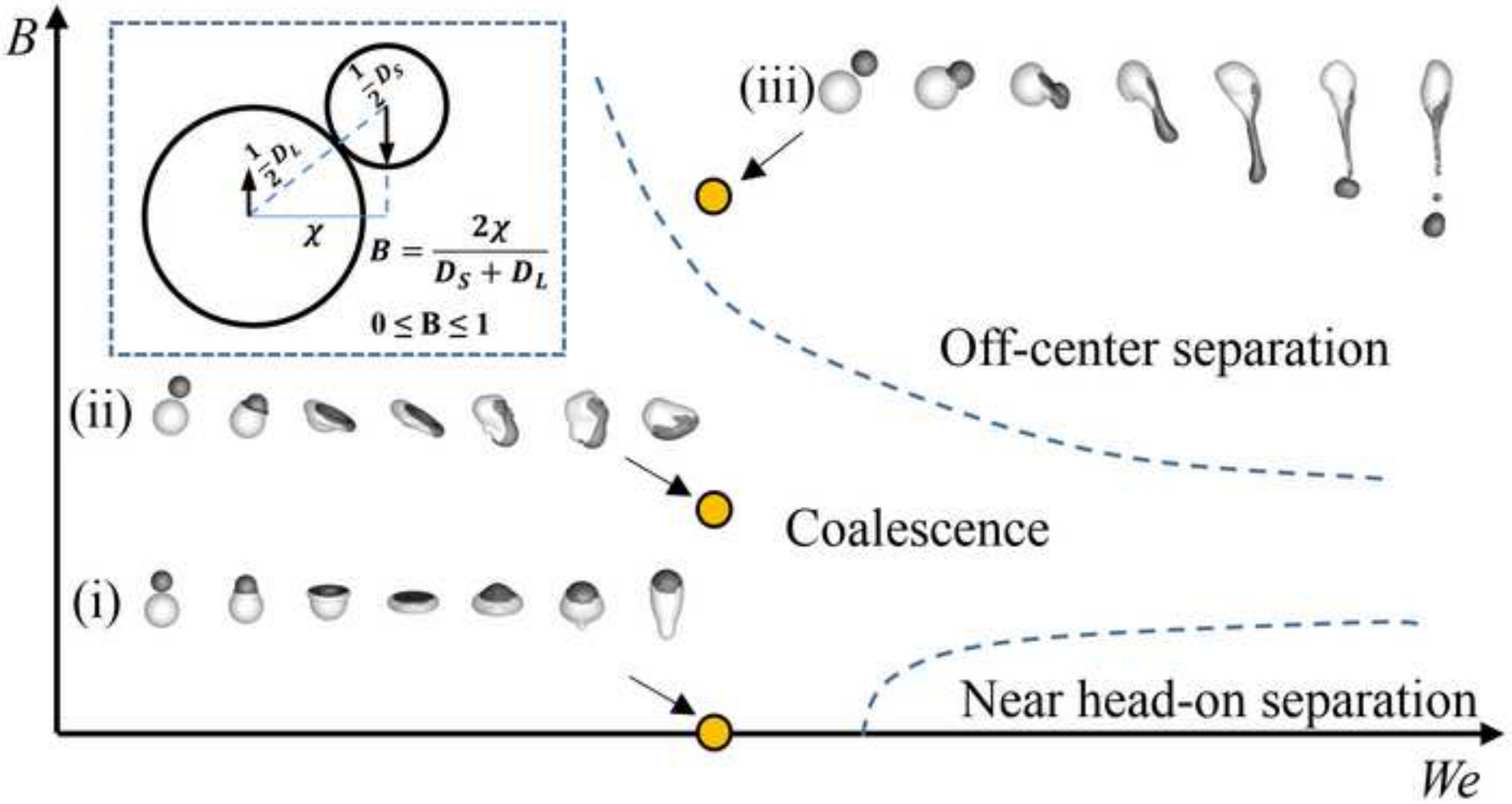

Figure 2

Click here to download high resolution image

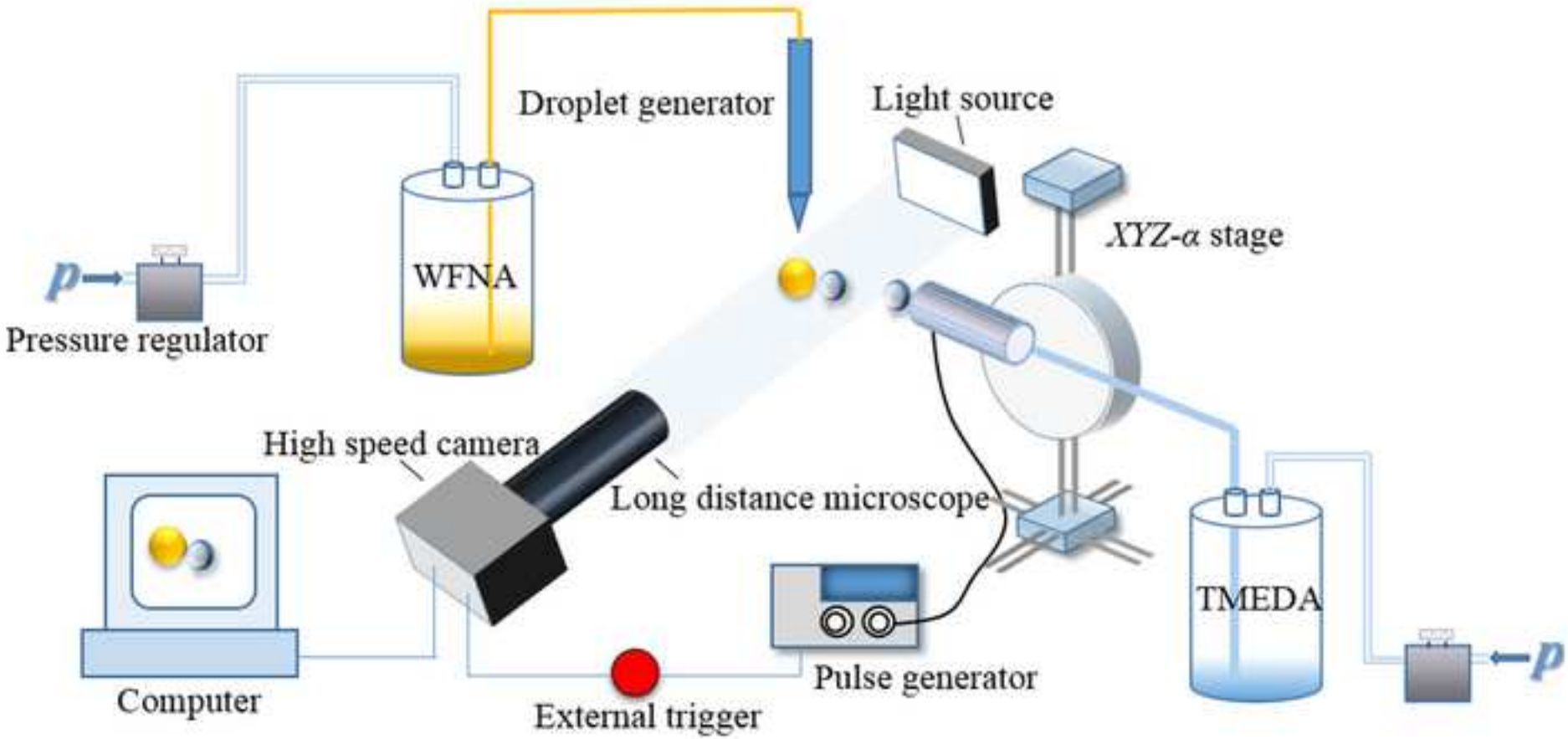

Figure 3

Click here to download high resolution image

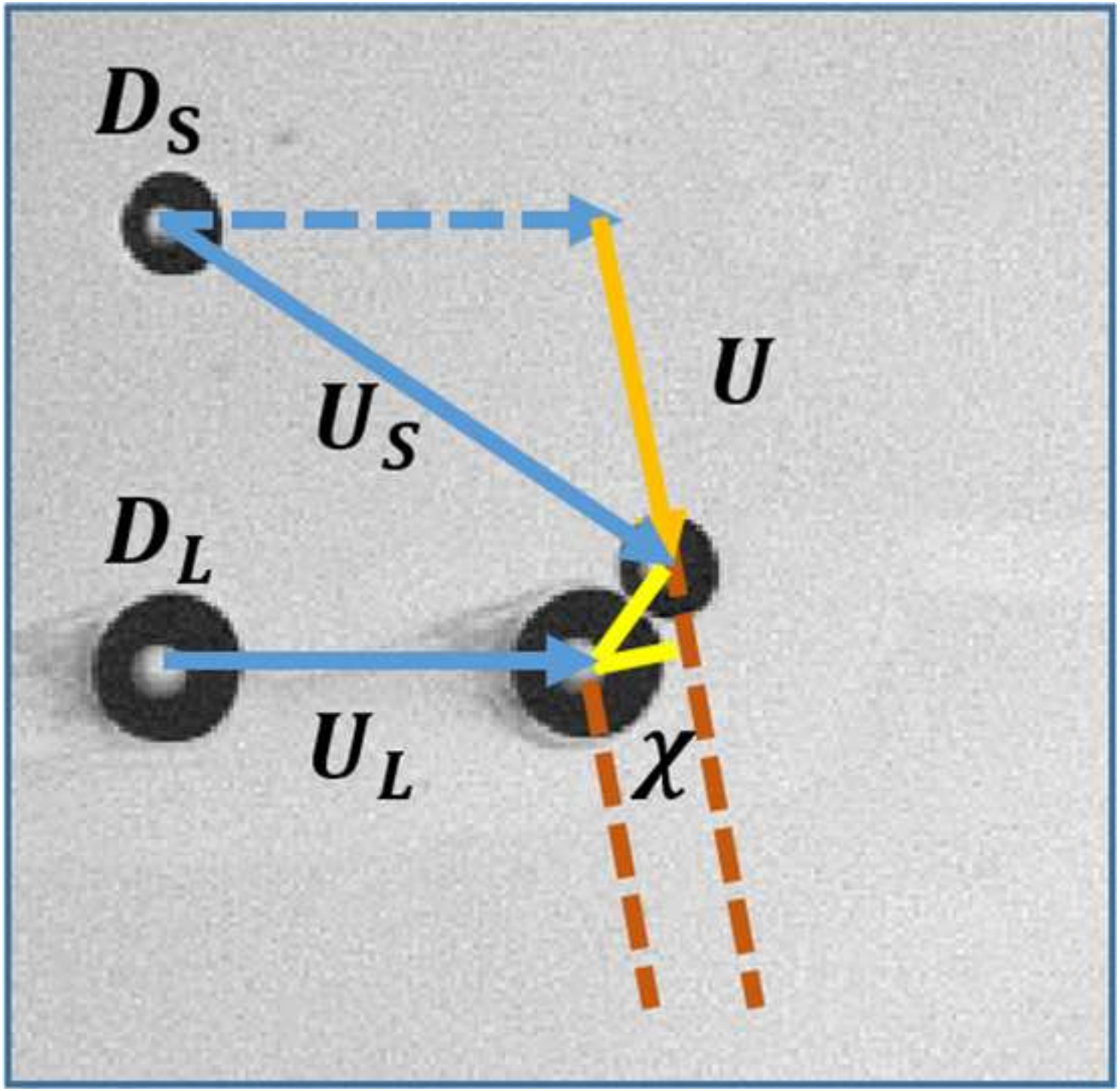

Figure 4

Click here to download high resolution image

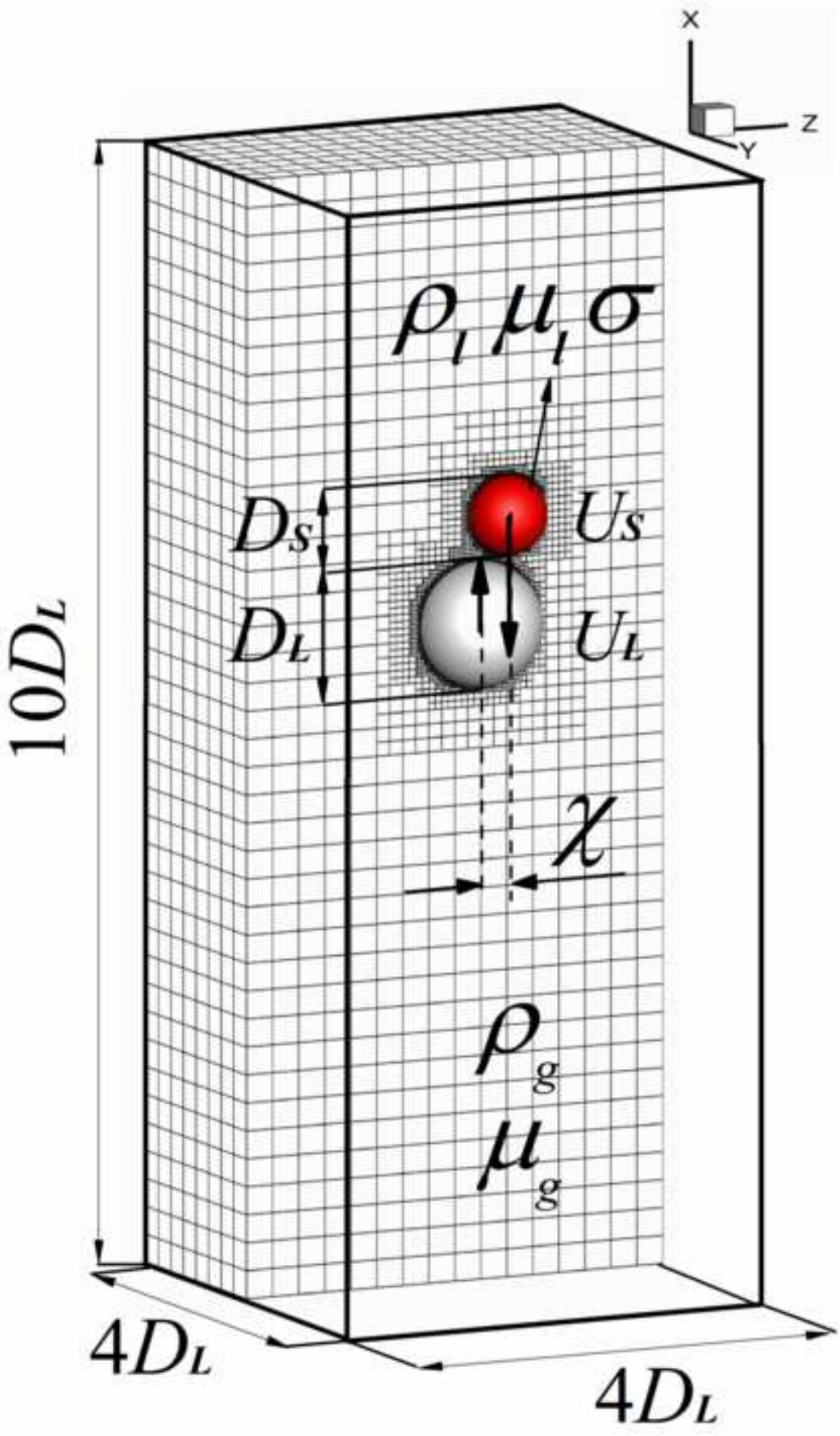

Figure 5

Click here to download high resolution image

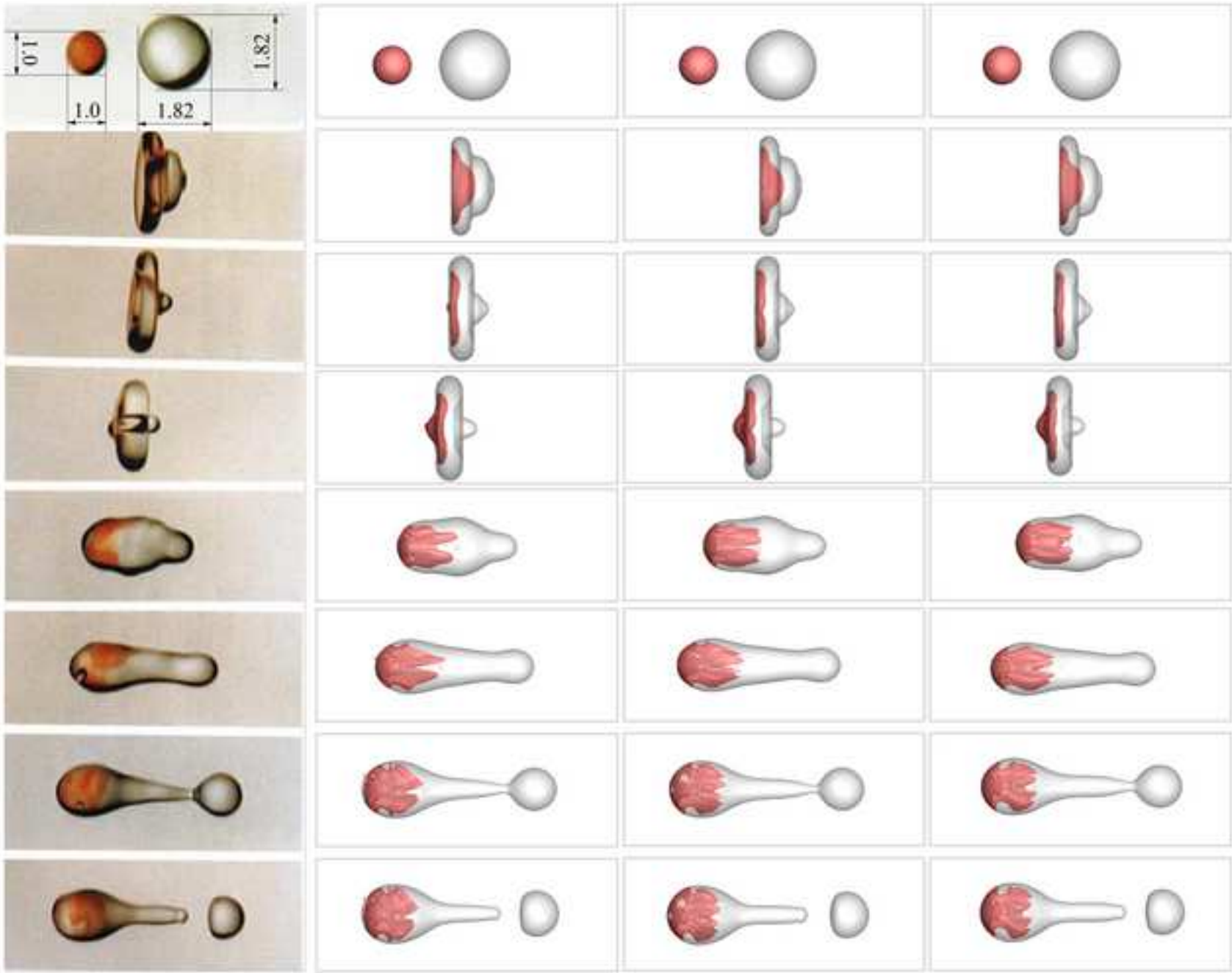

Figure 6

Click here to download high resolution image

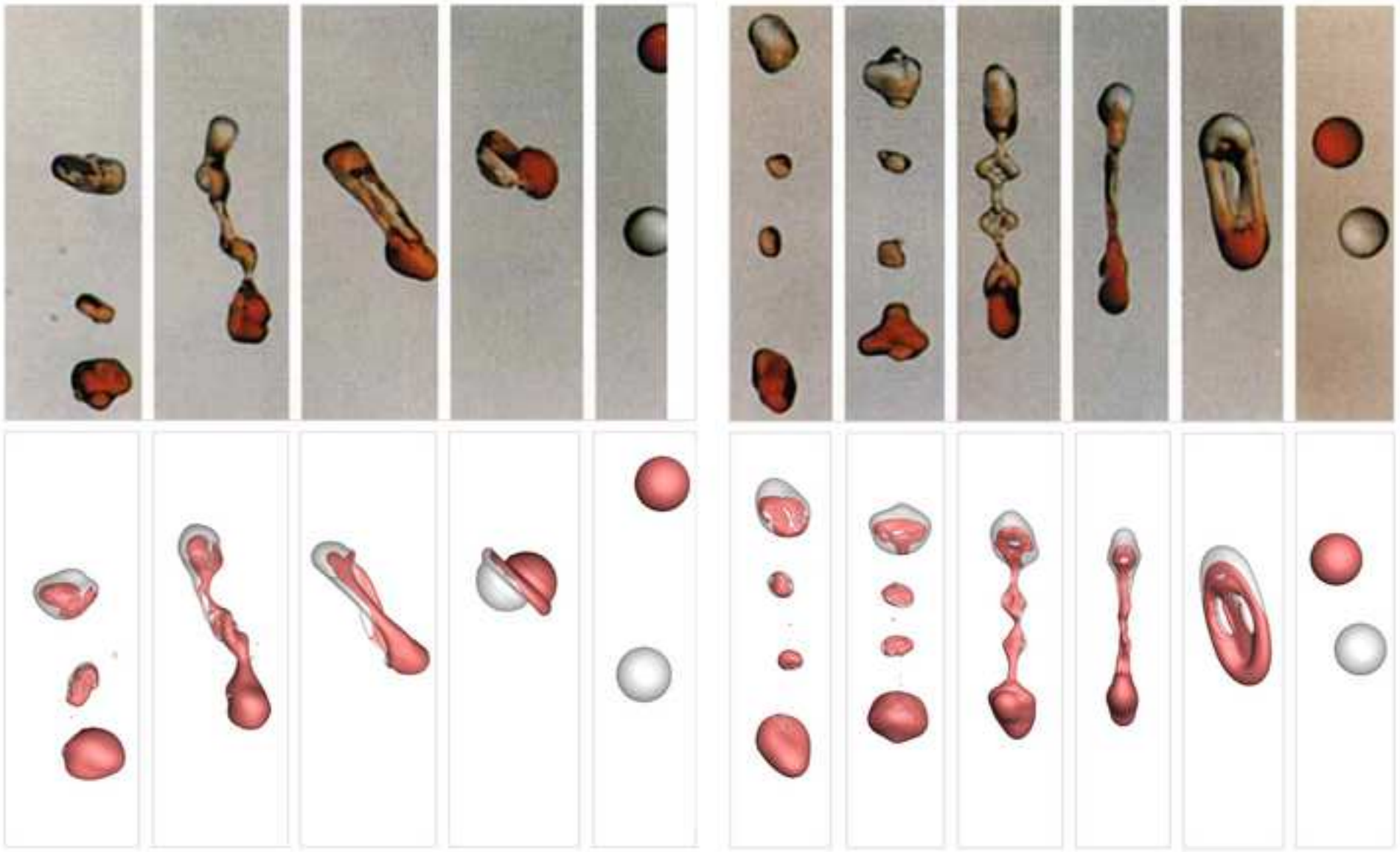

Figure 7

Click here to download high resolution image

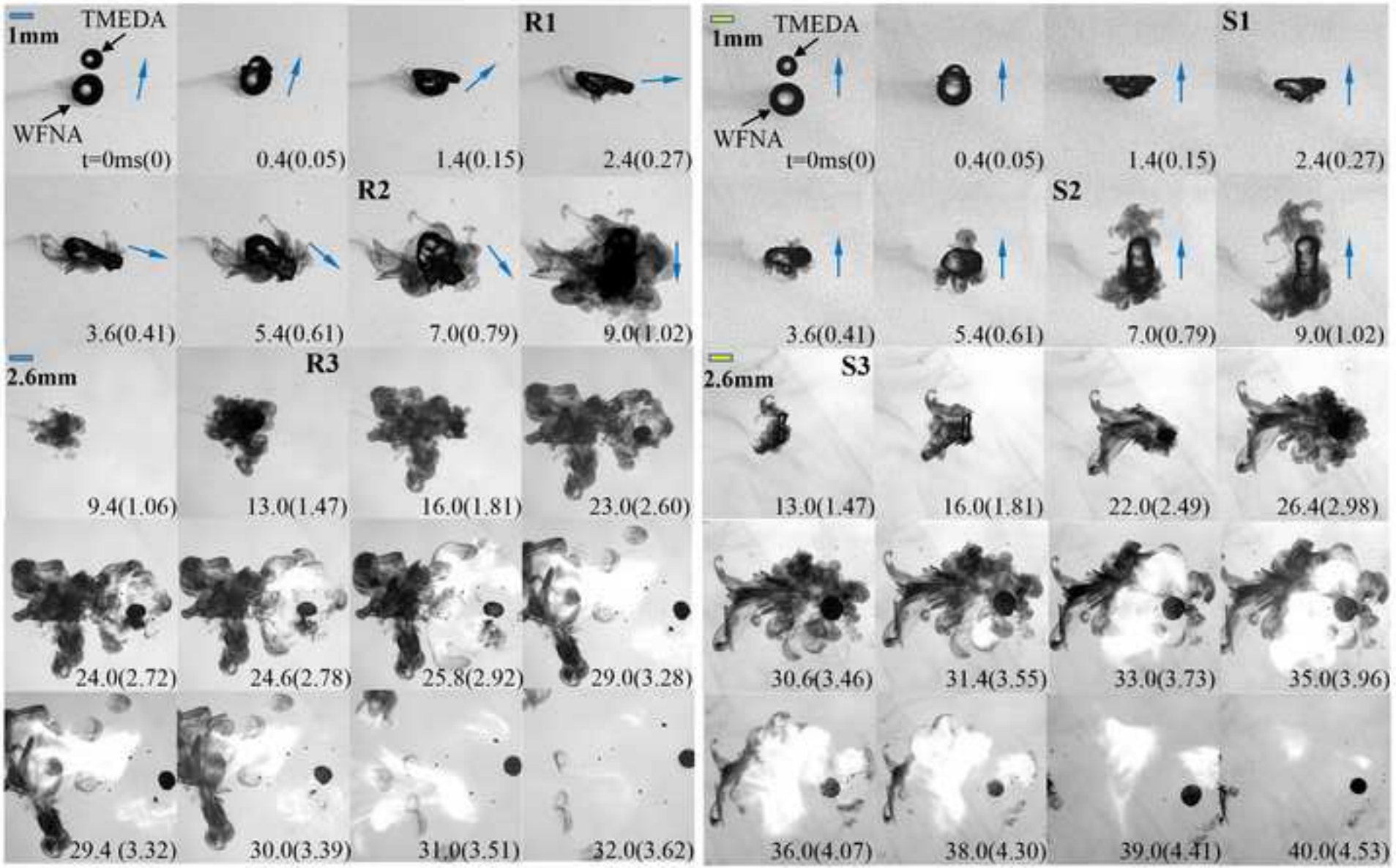

Figure 8

Click here to download high resolution image

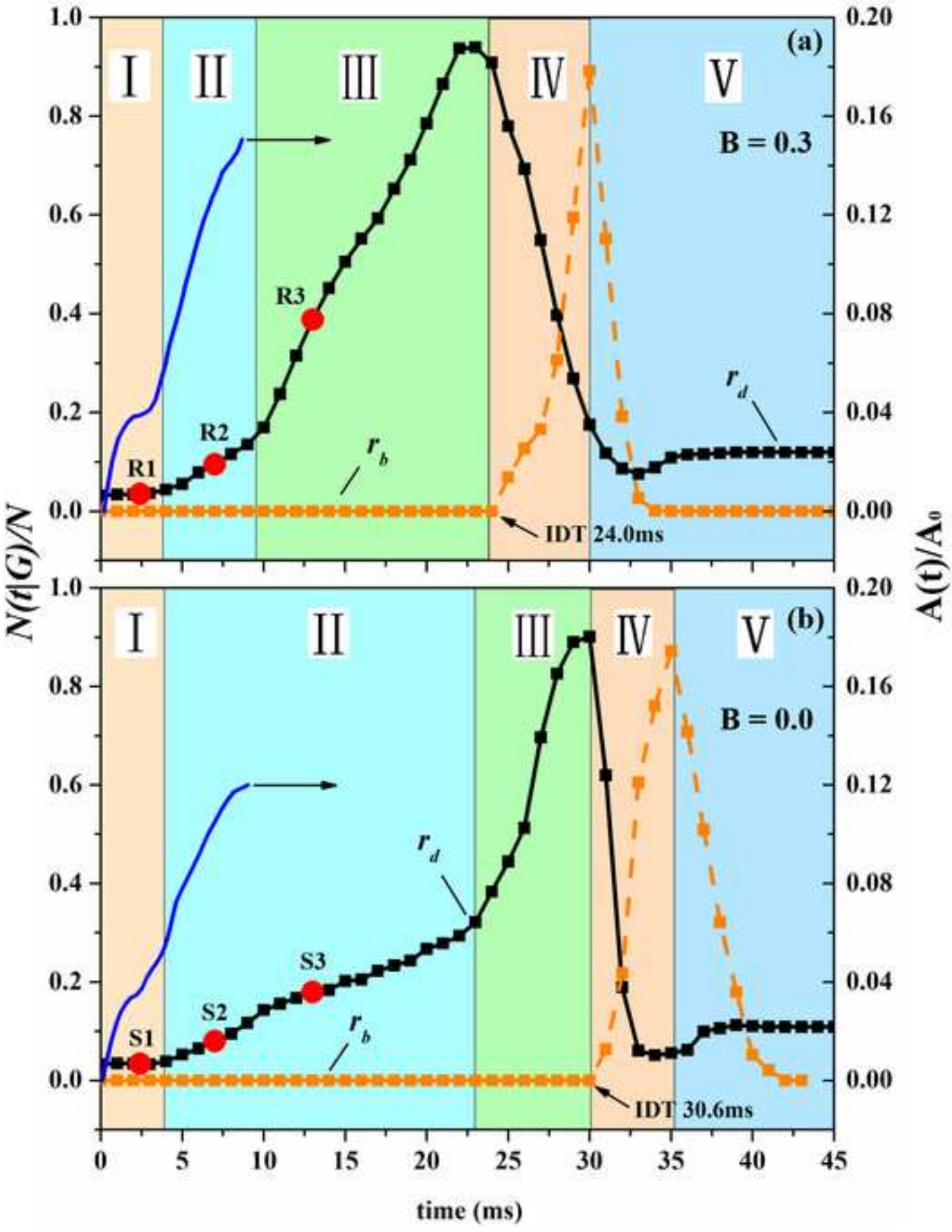

Figure 9

Click here to download high resolution image

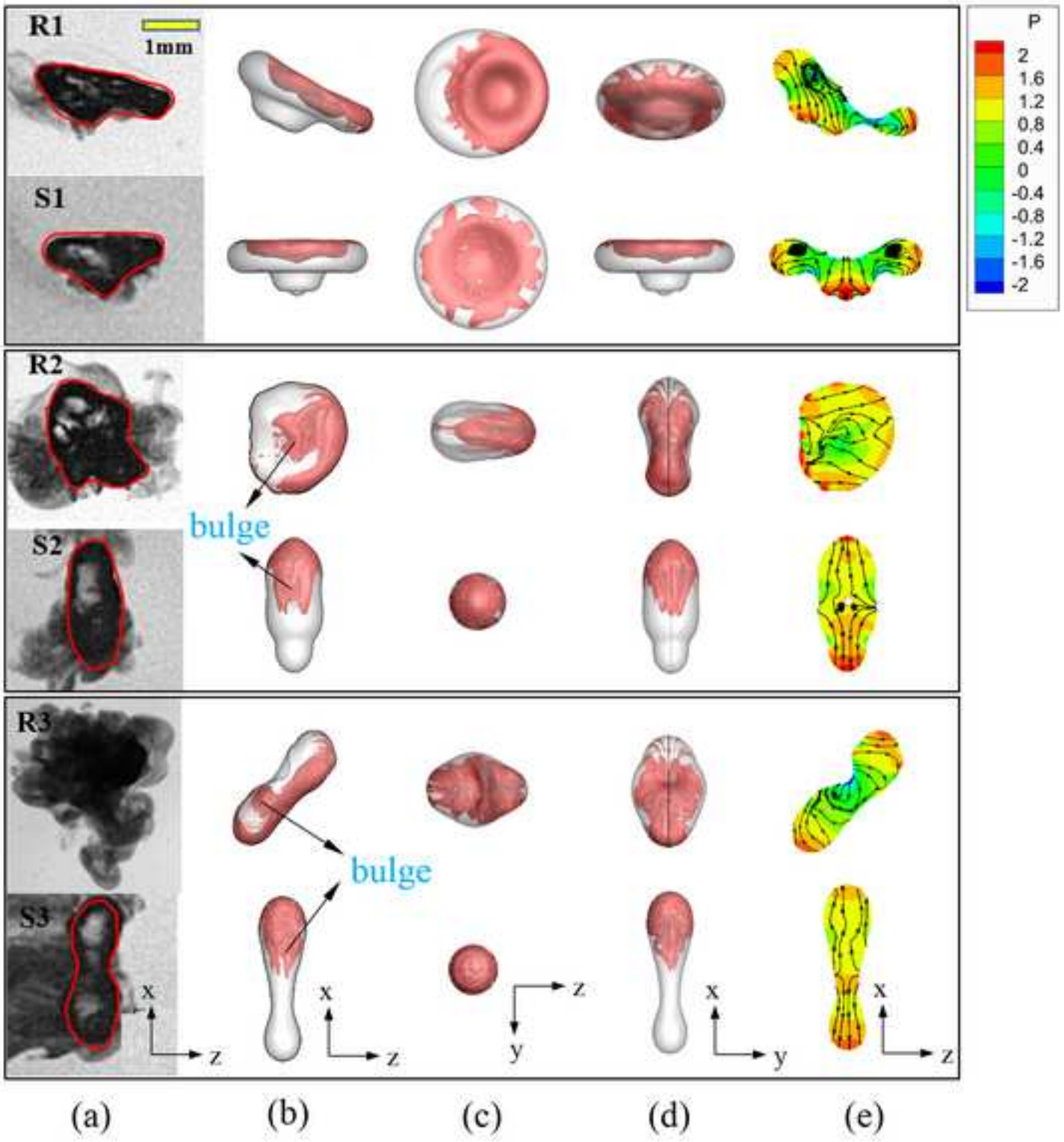

Figure 10

Click here to download high resolution image

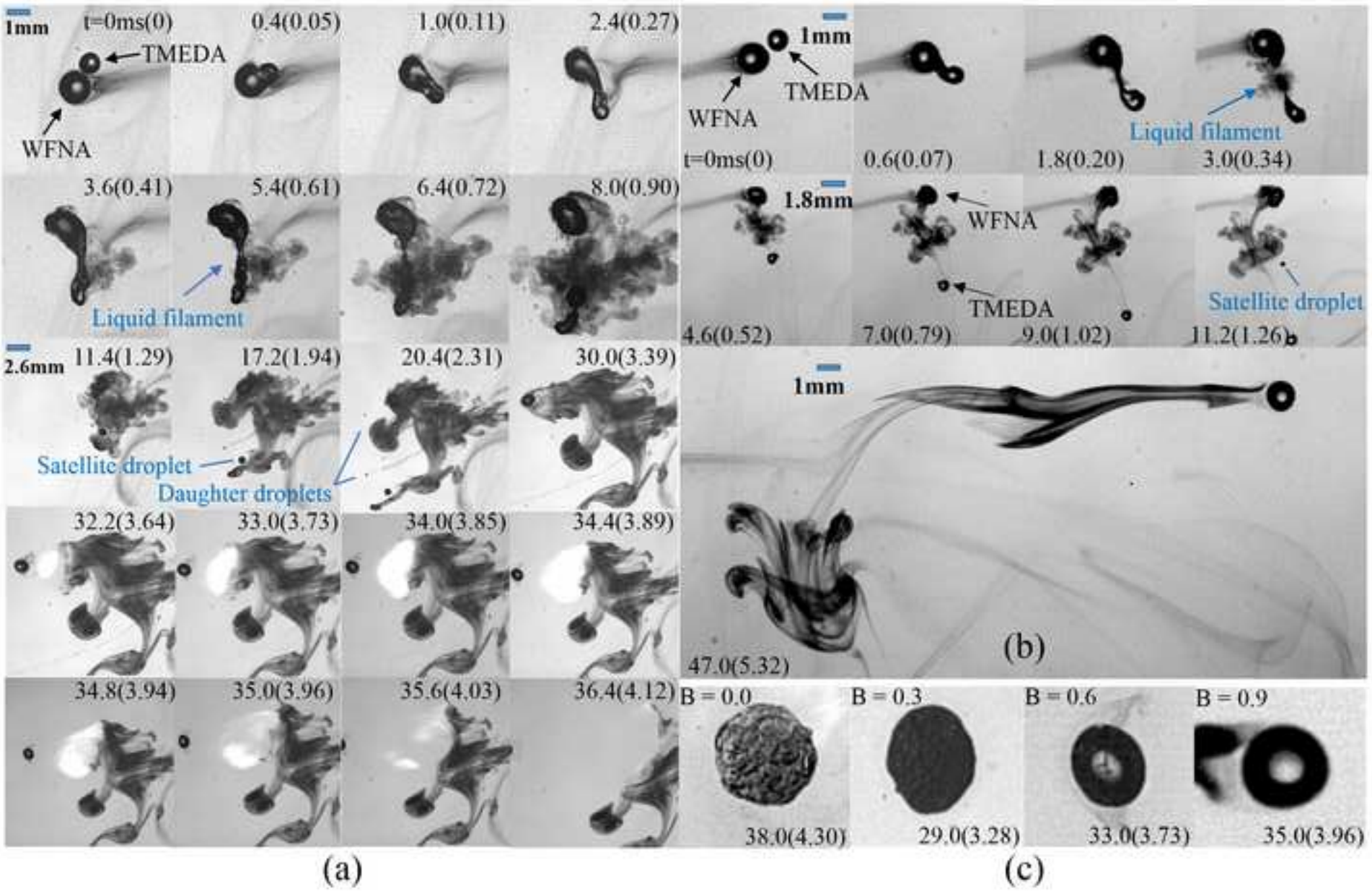

Figure 11

Click here to download high resolution image

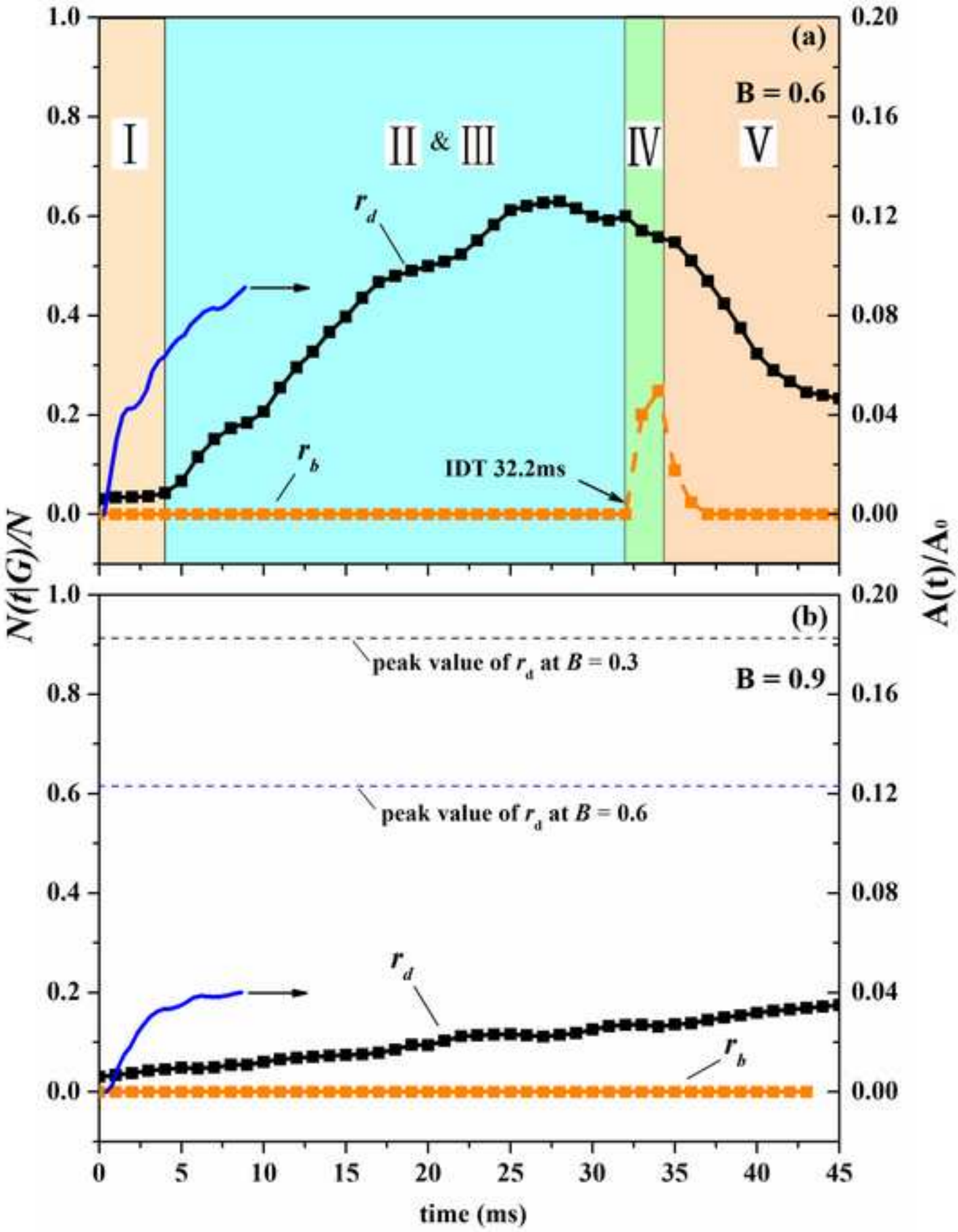

Figure 12

Click here to download high resolution image

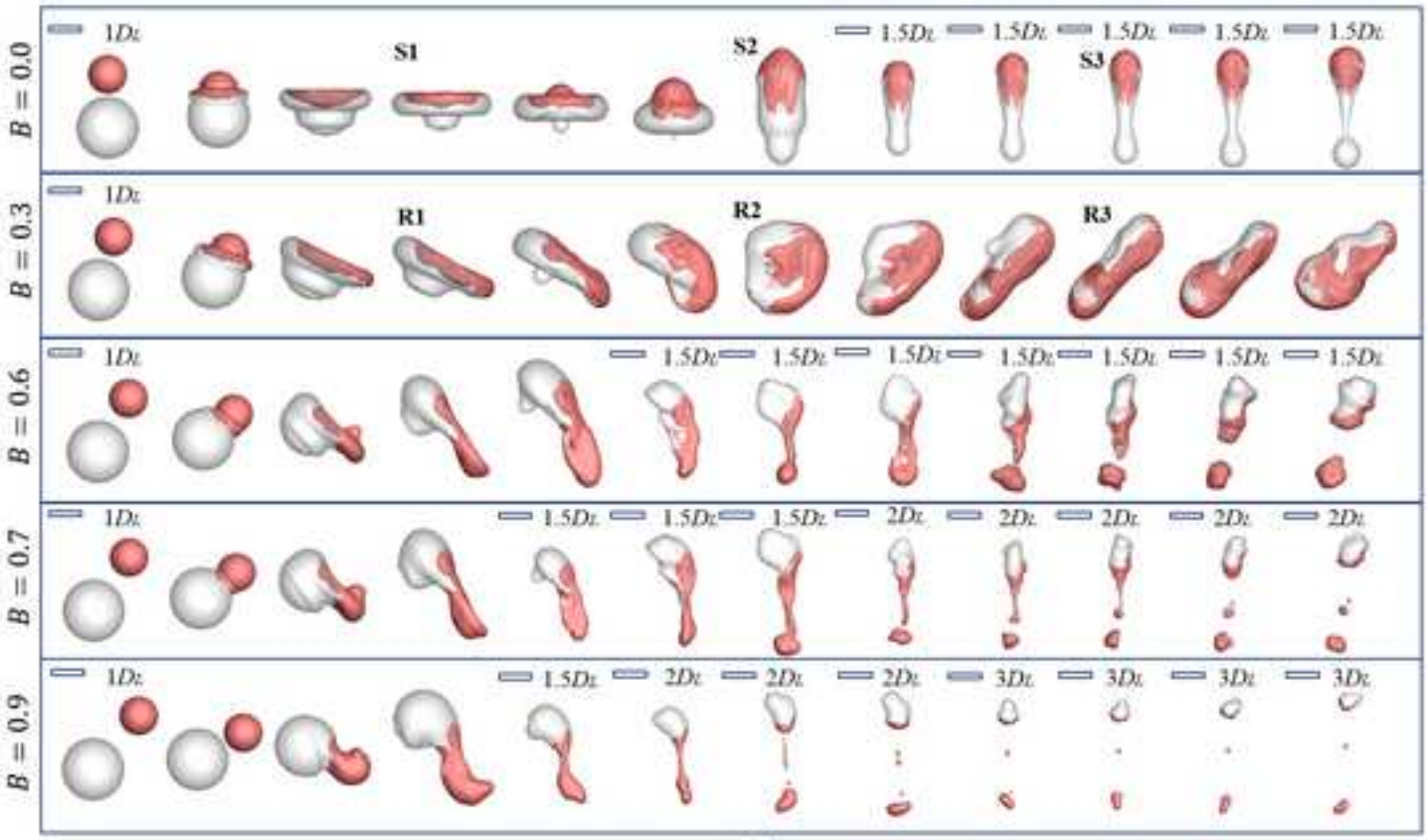

(a)

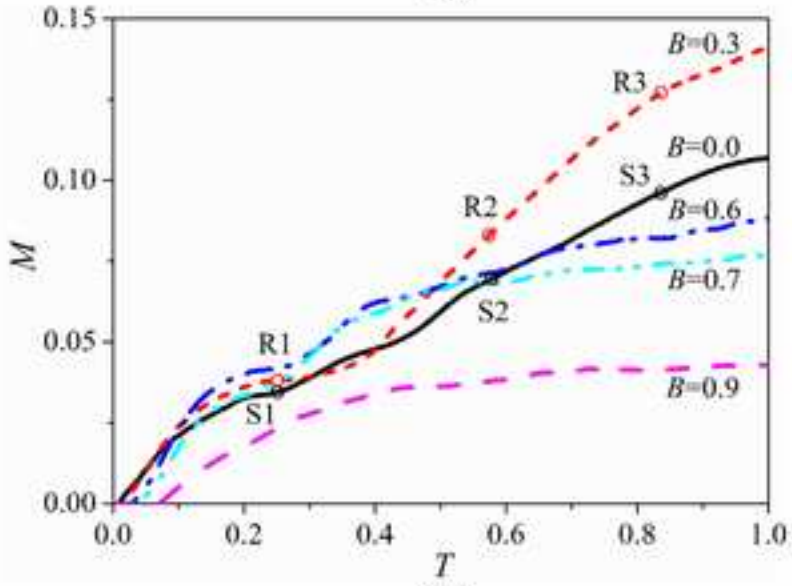

(b)

Figure 13

Click here to download high resolution image

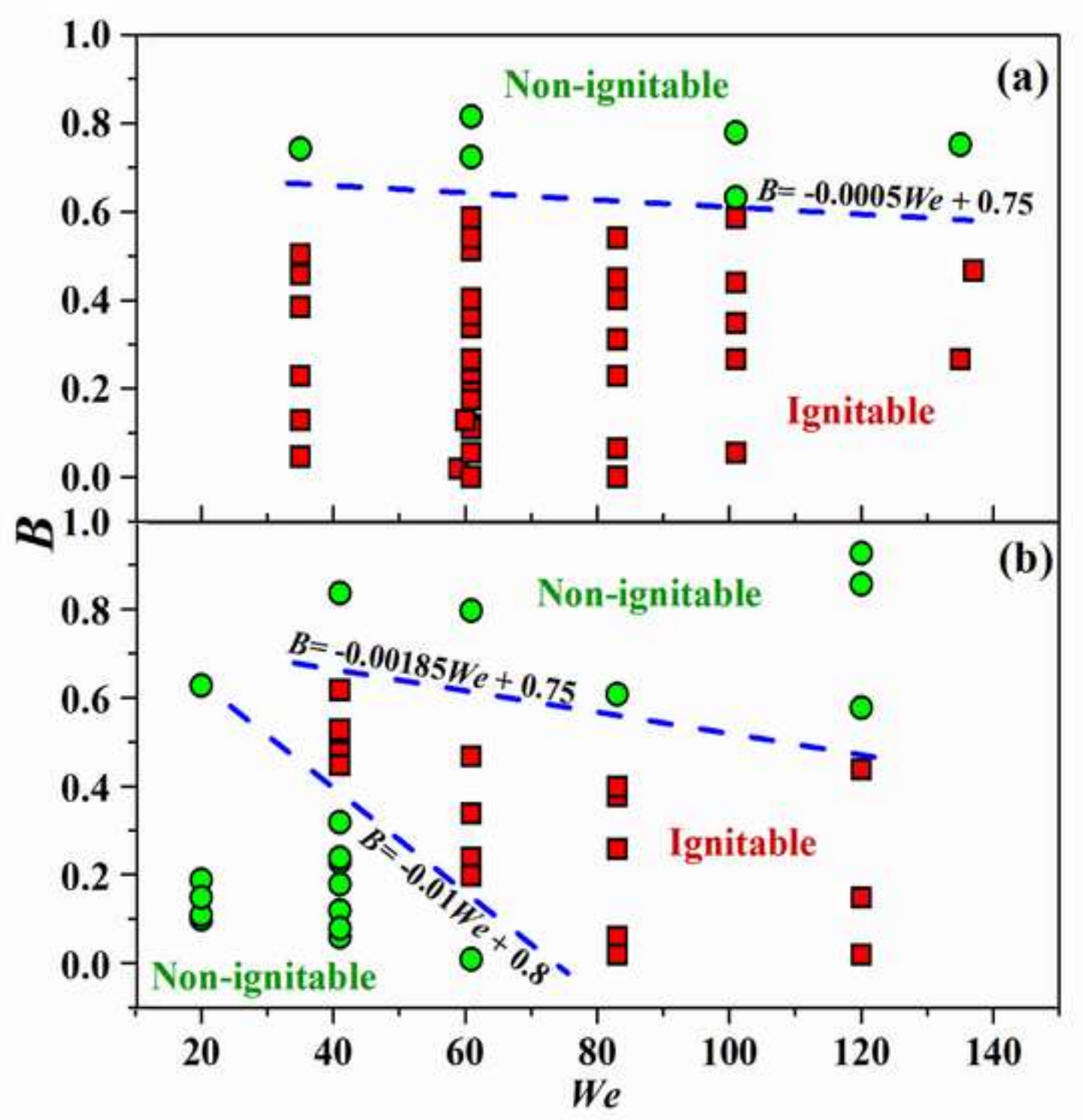

Figure 14

Click here to download high resolution image

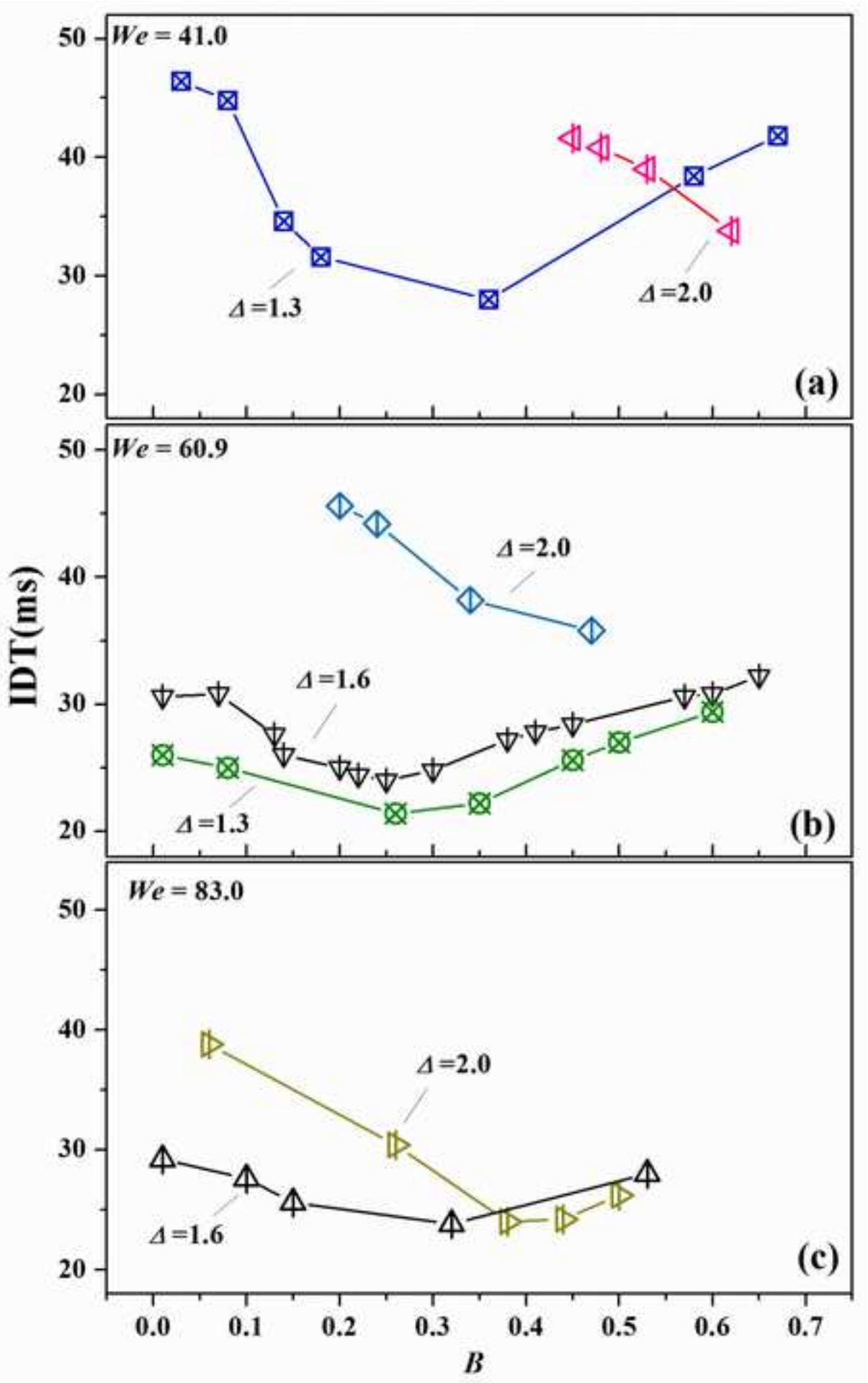

Supplementary Material

Click here to download Supplementary Material: Supplementary Materials.docx